Temperature dependence of the electronic structure of semiconductors and insulators

S. Poncé, Y. Gillet, J. Laflamme Janssen, A. Marini, M. Verstraete, and X. Gonze

Citation: The Journal of Chemical Physics **143**, 102813 (2015); doi: 10.1063/1.4927081
View online: http://dx.doi.org/10.1063/1.4927081
View Table of Contents: http://scitation.aip.org/content/aip/journal/jcp/143/10?ver=pdfcov
Published by the AIP Publishing

Temperature dependence of the electronic structure of semiconductors and insulators

S. Poncé,[1,a)] Y. Gillet,[1] J. Laflamme Janssen,[1] A. Marini,[2] M. Verstraete,[3] and X. Gonze[1]
[1]*European Theoretical Spectroscopy Facility and Institute of Condensed Matter and Nanosciences, Université catholique de Louvain, Chemin des étoiles 8, bte L07.03.01, B-1348 Louvain-la-neuve, Belgium*
[2]*Consiglio Nazionale delle Ricerche (CNR), Via Salaria Km 29.3, CP 10, 00016 Monterotondo Stazione, Italy*
[3]*European Theoretical Spectroscopy Facility and Physique des matériaux et nanostructures, Université de Liège, Allée du 6 Août 17, B-4000 Liège, Belgium*

(Received 21 April 2015; accepted 8 July 2015; published online 28 July 2015)

The renormalization of electronic eigenenergies due to electron-phonon coupling (temperature dependence and zero-point motion effect) is sizable in many materials with light atoms. This effect, often neglected in *ab initio* calculations, can be computed using the perturbation-based Allen-Heine-Cardona theory in the adiabatic or non-adiabatic harmonic approximation. After a short description of the recent progresses in this field and a brief overview of the theory, we focus on the issue of phonon wavevector sampling convergence, until now poorly understood. Indeed, the renormalization is obtained numerically through a slowly converging **q**-point integration. For non-zero Born effective charges, we show that a divergence appears in the electron-phonon matrix elements at $\mathbf{q} \to \Gamma$, leading to a divergence of the adiabatic renormalization at band extrema. This problem is exacerbated by the slow convergence of Born effective charges with electronic wavevector sampling, which leaves residual Born effective charges in *ab initio* calculations on materials that are physically devoid of such charges. Here, we propose a solution that improves this convergence. However, for materials where Born effective charges are physically non-zero, the divergence of the renormalization indicates a breakdown of the adiabatic harmonic approximation, which we assess here by switching to the non-adiabatic harmonic approximation. Also, we study the convergence behavior of the renormalization and develop reliable extrapolation schemes to obtain the converged results. Finally, the adiabatic and non-adiabatic theories, with corrections for the slow Born effective charge convergence problem (and the associated divergence) are applied to the study of five semiconductors and insulators: α-AlN, β-AlN, BN, diamond, and silicon. For these five materials, we present the zero-point renormalization, temperature dependence, phonon-induced lifetime broadening, and the renormalized electronic band structure. © *2015 AIP Publishing LLC.* [http://dx.doi.org/10.1063/1.4927081]

I. INTRODUCTION

State-of-the-art accurate calculations of the electronic structure of solids rely often on a combination of density functional theory (DFT)[1,2] and many-body perturbation theory (MBPT).[3,4] Usually, DFT provides reliable initial starting wave functions and valence eigenenergies, but poor bandgap. The DFT wavefunctions are then post-treated by MBPT in the so-called GW approximation.[5] Such a combined approach delivers electronic bandgaps within 0.1-0.4 eV of the experimental ones.[6,7] For many weakly correlated materials, one-shot GW corrections to DFT are sufficient to reach this agreement, while self-consistent GW is needed for more strongly correlated materials. The GW corrections to the DFT bandgap can be as large as a few eV, i.e., 2 eV for the direct gap of diamond.[8,9] For the accurate description of optical properties, the treatment of excitonic effects is important, which can be done on the basis of the Bethe-Salpeter equation (BSE),[10] using the GW band structure as input.

This well-established DFT+MBPT approach neglects electron-phonon coupling and is thus unable to predict temperature-dependent modification of the electronic band structure, as well as corrections already present at 0 K, due to the zero-point motion. Those are arguably the next largest corrections to the electronic states description, at least for materials that contain light nuclei. As a paradigmatic example, for the direct bandgap of diamond, the zero-point motion correction is as large as 0.6 eV.[8,9]

The treatment of the effect of electron-phonon coupling on the electronic structure has a long and chaotic history that started in the early 1950s. For a historical review, the reader is invited to consult Ref. 11. Over the years, computations have relied on three types of methods, with different advantages and drawbacks: (1) as a time average of the bandgap using first-principles molecular dynamics (MD) simulations, (2) through the frozen-phonon (FP) method, which weights the eigenenergy change along the phonon modes with a Bose-Einstein distribution, and (3) thanks to the diagrammatic method of many-body perturbation theory. These three types of methods are compared to each other, at the harmonic level, in Ref. 11.

a)Electronic mail: samuel.pon@gmail.com

In the present contribution, we rely on the Allen-Heine-Cardona (AHC) theory[12–14] to compute the zero-point motion renormalization (ZPR) as well as the temperature dependence of electronic eigenenergies. The AHC theory originates from the diagrammatic method of many-body perturbation theory. It has been applied in several recent contributions in the field, including the computation of temperature-dependence of the optical properties,[15] the computation of the surprisingly large ZPR of the diamond bandgap,[8,16] the demonstration of large non-rigid ion corrections for molecules,[17] the inclusion of dynamical effects beyond the adiabatic approximation,[18–20] the study of the anharmonic electron-phonon contribution to the indirect bandgap of diamond,[21] and the inclusion of electronic many-body effects (in the GW approximation) in the ZPR of diamond,[9] noticing a large increase of the renormalization with respect to DFT. Also, we believe that the confusion in the theoretical understanding of the relationship between MD, FP, and AHC as well as the inaccuracies in first-principles software implementations of AHC has been largely eliminated in two recent publications.[11,16]

One of the major issues when performing AHC calculations is the slow convergence with respect to phonon wavevector sampling of the Brillouin Zone (BZ),[16] referred to as **q**-point sampling from now on. To accelerate this convergence, a small imaginary component $i\delta$ (which can be inferred as a finite lifetime for the unoccupied electronic states due to thermal effects) is often used. However, this imaginary parameter is *ad hoc* rather than *ab initio*. Also, the convergence problem becomes critical with the MD and FP methods, as supercells must be used to sample the phonon wavevectors, thus dramatically increasing the computational time and memory required. Currently, numerical convergence for the MD and FP methods cannot reliably be reached in three-dimensional solids, in contrast with finite systems.[9,16,22]

In this paper, we highlight that in AHC simulations, the ZPR diverges at dense **q**-point samplings and vanishing $i\delta$. For materials with no infrared (IR) active phonon modes (which we will refer to as IR-inactive materials in the remainder of this paper), such unphysical divergence is attributed to a residual Born effective charge, which stems from the finite **k**-point sampling. We propose a solution to this problem and devise a systematic way to converge the ZPR for vanishing $i\delta$. For IR-active materials (i.e., materials with IR active phonon modes), the problem is more fundamental. Indeed, the divergence in the adiabatic AHC approach is not simply numerical and indicates a breakdown of the AHC approach. Resorting to the non-adiabatic AHC theory solves this issue.

This paper is organized as follows. First, a short reminder of the AHC theory is presented in Section II. In Section III, the bottleneck of the **q**-point convergence is discussed, the divergence problem of the ZPR at large **q**-point density is explored and a solution is proposed. We also devise in Sections IV and V a systematic way to extrapolate the ZPR at infinite **q**-point density and vanishing $i\delta$. Finally, in Section VI, we present the temperature dependences, the ZPR, and the phonon-induced lifetimes for five semiconductors: α-AlN, β-AlN, BN, diamond, and silicon. Atomic units are used throughout.

II. REVIEW OF THE ALLEN-HEINE-CARDONA FORMALISM

A. The AHC theory within the adiabatic harmonic approximation

The temperature-dependent renormalization of the electronic eigenenergy $\varepsilon_{n\mathbf{k}}$ for band n and wavevector $\mathbf{k}$ can be written in the adiabatic harmonic approximation as a sum over the BZ of the phonon contributions for each wavevector $\mathbf{q}$,[11]

$$\Delta\varepsilon_{n\mathbf{k}}(T) = \frac{1}{N_q}\sum_{\mathbf{q}}\sum_{m}^{3N}\frac{\partial\varepsilon_{n\mathbf{k}}}{\partial n_{m\mathbf{q}}}\left(n_{m\mathbf{q}}(T)+\frac{1}{2}\right), \tag{1}$$

with

$$\frac{\partial\varepsilon_{n\mathbf{k}}}{\partial n_{m\mathbf{q}}} = \frac{1}{2\omega_{m\mathbf{q}}}\sum_{\substack{\kappa\alpha\\ \kappa'\gamma}}\sum_{ll'}\frac{\partial^2\varepsilon_{n\mathbf{k}}}{\partial R_{l\kappa\alpha}\partial R_{l'\kappa'\gamma}} \times e^{-i\mathbf{q}\cdot(\mathbf{R}_l-\mathbf{R}_{l'})}U^*_{m,\kappa'\gamma}(\mathbf{q})U_{m,\kappa\alpha}(\mathbf{q}), \tag{2}$$

where m is the phonon branch, T is the temperature, N_q is the number of wavevectors used to sample the BZ, $\omega_{m\mathbf{q}}$ is the phonon frequency, $n_{m\mathbf{q}}(T) = \frac{1}{e^{\frac{\omega_{m\mathbf{q}}}{k_BT}}-1}$ is the Bose-Einstein distribution, $U_{m,\kappa\alpha}(\mathbf{q})$ is the eigendisplacement vector of atom κ in direction α associated to the phonon mode m, and $\partial/\partial R_{l\kappa\alpha}$ is the derivative of a quantity with respect to the displacement of atom κ of the unit cell l in the direction α.

The quantity $\Delta\varepsilon_{n\mathbf{k}}(T) \triangleq \varepsilon_{n\mathbf{k}}(T) - \varepsilon_{n\mathbf{k}}[0]$ is the difference between the temperature-dependent eigenenergy and the eigenenergy at ground-state atomic positions. We distinguish the temperature-dependent $\varepsilon_{n\mathbf{k}}$ from the atomic-position-dependent $\varepsilon_{n\mathbf{k}}$ by using () in the former and [] in the latter. The difference between $\varepsilon_{n\mathbf{k}}(T=0)$ and $\varepsilon_{n\mathbf{k}}[0]$ is called the ZPR.

In a mean-field approximation like the DFT, the eigenenergies are the expectation values of the Hamiltonian $\hat{H}_{\mathbf{k},\mathbf{k}}$ of the system

$$\varepsilon_{n\mathbf{k}} = \left\langle u^{(0)}_{n\mathbf{k}}\right| \hat{H}_{\mathbf{k},\mathbf{k}} \left|u^{(0)}_{n\mathbf{k}}\right\rangle, \tag{3}$$

with $u^{(0)}_{n\mathbf{k}}$ the periodic part of the electronic wavefunctions. Using perturbation theory to obtain the second-order derivative with respect to atomic displacements of such eigenenergies, Eq. (2) can be rewritten as

$$\frac{\partial\varepsilon_{n\mathbf{k}}}{\partial n_{m\mathbf{q}}} = \frac{1}{2\omega_{m\mathbf{q}}}\sum_{\substack{\kappa\alpha\\ \kappa'\gamma}}U^*_{m,\kappa'\gamma}(\mathbf{q})U_{m,\kappa\alpha}(\mathbf{q}) \times\Bigg\{\left\langle u^{(0)}_{n\mathbf{k}}\right|\frac{\partial^2\hat{H}_{\mathbf{k},\mathbf{k}}}{\partial R_{\kappa\alpha}(-\mathbf{q})\partial R_{\kappa'\gamma}(\mathbf{q})}\left|u^{(0)}_{n\mathbf{k}}\right\rangle + \frac{1}{2}\Bigg(\left(\left\langle\frac{\partial u_{n\mathbf{k}}}{\partial R_{\kappa\alpha}(\mathbf{q})}\right|\frac{\partial\hat{H}_{\mathbf{k},\mathbf{k}}}{\partial R_{\kappa'\gamma}(\mathbf{q})}\left|u^{(0)}_{n\mathbf{k}}\right\rangle + (\kappa\alpha)\leftrightarrow(\kappa'\gamma)\right) + (c.c.)\Bigg)\Bigg\}, \tag{4}$$

where $(c.c.)$ stands for the complex conjugate of the previous terms within parentheses, and where we use the following notation for the derivative with respect to atomic positions of an arbitrary quantity X:

$$\frac{\partial X}{\partial R_{\kappa\alpha}(\mathbf{q})} = \frac{1}{N_{BvK}}\sum_{l}e^{i\mathbf{q}\cdot\mathbf{R}_l}\frac{\partial X}{\partial R_{l\kappa\alpha}}, \tag{5}$$

N_{BvK} being the number of primitive cells of the periodic system defined by the Born-von Kármán boundary conditions.[23]

The first term within curly brackets in Eq. (4) is called the Debye-Waller (DW) term,

$$\mathcal{D}^{\kappa\alpha}_{\kappa'\gamma}(\mathbf{q}) \triangleq \left\langle u^{(0)}_{n\mathbf{k}} \middle| \frac{\partial^2 \hat{H}_{\mathbf{k},\mathbf{k}}}{\partial R_{\kappa\alpha}(-\mathbf{q}) \partial R_{\kappa'\gamma}(\mathbf{q})} \middle| u^{(0)}_{n\mathbf{k}} \right\rangle, \tag{6}$$

while the remainder constitutes the Fan term,

$$\mathcal{F}^{\kappa\alpha}_{\kappa'\gamma}(\mathbf{q}) \triangleq \frac{1}{2}\left(\left(\left\langle \frac{\partial u_{n\mathbf{k}}}{\partial R_{\kappa\alpha}(\mathbf{q})} \middle| \frac{\partial \hat{H}_{\mathbf{k},\mathbf{k}}}{\partial R_{\kappa'\gamma}(\mathbf{q})} \middle| u^{(0)}_{n\mathbf{k}} \right\rangle + (\kappa\alpha) \leftrightarrow (\kappa'\gamma) \right) + (c.c.) \right). \tag{7}$$

The change of eigenenergy $\varepsilon_{n\mathbf{k}}$ due to the specific phonon mode m with wavevector $\mathbf{q}$ (Eq. (4)) thus becomes

$$\frac{\partial \varepsilon_{n\mathbf{k}}}{\partial n_{m\mathbf{q}}} \triangleq \frac{\partial \varepsilon^{\mathrm{FAN}}_{n\mathbf{k}}}{\partial n_{m\mathbf{q}}} + \frac{\partial \varepsilon^{\mathrm{DW}}_{n\mathbf{k}}}{\partial n_{m\mathbf{q}}}, \tag{8}$$

with the Fan contribution given by

$$\frac{\partial \varepsilon^{\mathrm{FAN}}_{n\mathbf{k}}}{\partial n_{m\mathbf{q}}} \triangleq \frac{1}{2\omega_{m\mathbf{q}}} \sum_{\substack{\kappa\alpha \\ \kappa'\gamma}} \mathcal{F}^{\kappa\alpha}_{\kappa'\gamma}(\mathbf{q}) U^*_{m,\kappa'\gamma}(\mathbf{q}) U_{m,\kappa\alpha}(\mathbf{q}) \tag{9}$$

and the Debye-Waller contribution given by

$$\frac{\partial \varepsilon^{\mathrm{DW}}_{n\mathbf{k}}}{\partial n_{m\mathbf{q}}} \triangleq \frac{1}{2\omega_{m\mathbf{q}}} \sum_{\substack{\kappa\alpha \\ \kappa'\gamma}} \mathcal{D}^{\kappa\alpha}_{\kappa'\gamma}(\mathbf{q}) U^*_{m,\kappa'\gamma}(\mathbf{q}) U_{m,\kappa\alpha}(\mathbf{q}). \tag{10}$$

At this point, no approximations beyond the adiabatic and harmonic ones were made. However, the calculation of the Debye-Waller term (Eq. (6)) requires the second-order derivative of the Hamiltonian, which is a computational bottleneck within the density functional perturbation theory (DFPT) framework. To overcome this issue, we make the rigid-ion approximation (RIA), a standard approach within the AHC framework[12–14] that allows the renormalization to be computed from first-order derivatives of the Hamiltonians only

$$\frac{\partial \varepsilon^{\mathrm{DW_{RIA}}}_{n\mathbf{k}}}{\partial n_{m\mathbf{q}}} = \frac{-1}{4\omega_{m\mathbf{q}}} \sum_{\substack{\kappa\alpha \\ \kappa'\gamma}} \mathcal{F}^{\kappa\alpha}_{\kappa'\gamma}(\mathbf{\Gamma}) \left(U^*_{m,\kappa\gamma}(\mathbf{q}) U_{m,\kappa\alpha}(\mathbf{q}) + U^*_{m,\kappa'\gamma}(\mathbf{q}) U_{m,\kappa'\alpha}(\mathbf{q}) \right). \tag{11}$$

We thus split the DW term into RIA and non-RIA (NRIA) contributions,

$$\frac{\partial \varepsilon^{\mathrm{DW}}_{n\mathbf{k}}}{\partial n_{m\mathbf{q}}} = \frac{\partial \varepsilon^{\mathrm{DW_{RIA}}}_{n\mathbf{k}}}{\partial n_{m\mathbf{q}}} + \frac{\partial \varepsilon^{\mathrm{DW_{NRIA}}}_{n\mathbf{k}}}{\partial n_{m\mathbf{q}}}, \tag{12}$$

with

$$\frac{\partial \varepsilon^{\mathrm{DW_{NRIA}}}_{n\mathbf{k}}}{\partial n_{m\mathbf{q}}} = \frac{1}{2\omega_{m\mathbf{q}}} \sum_{\substack{\kappa\alpha \\ \kappa'\gamma}} \left[\mathcal{D}^{\kappa\alpha}_{\kappa'\gamma}(\mathbf{q}) U^*_{m,\kappa'\gamma}(\mathbf{q}) U_{m,\kappa\alpha}(\mathbf{q}) + \frac{1}{2} \mathcal{F}^{\kappa\alpha}_{\kappa'\gamma}(\mathbf{\Gamma}) \times \left(U^*_{m,\kappa\gamma}(\mathbf{q}) U_{m,\kappa\alpha}(\mathbf{q}) + U^*_{m,\kappa'\gamma}(\mathbf{q}) U_{m,\kappa'\alpha}(\mathbf{q}) \right) \right]. \tag{13}$$

Also, in our calculations, all Fan-like contributions are obtained within DFPT and can thus be written as follows:

$$\left\langle \frac{\partial u_{n\mathbf{k}}}{\partial R_{\kappa\alpha}(\mathbf{q})} \middle| \frac{\partial \hat{H}_{\mathbf{k},\mathbf{k}}}{\partial R_{\kappa'\gamma}(\mathbf{q})} \middle| u^{(0)}_{n\mathbf{k}} \right\rangle = \sum_{n'=1}^{M}{}' \frac{\left\langle u^{(0)}_{n\mathbf{k}} \middle| \frac{\partial \hat{H}_{\mathbf{k},\mathbf{k}}}{\partial R_{\kappa\alpha}(-\mathbf{q})} \middle| u^{(0)}_{n'\mathbf{k}+\mathbf{q}} \right\rangle \left\langle u^{(0)}_{n'\mathbf{k}+\mathbf{q}} \middle| \frac{\partial \hat{H}_{\mathbf{k},\mathbf{k}}}{\partial R_{\kappa'\gamma}(\mathbf{q})} \middle| u^{(0)}_{n\mathbf{k}} \right\rangle}{\varepsilon^{(0)}_{n\mathbf{k}} - \varepsilon^{(0)}_{n'\mathbf{k}+\mathbf{q}}} + \left\langle \hat{P}_{c\mathbf{k}+\mathbf{q}} \frac{\partial u_{n\mathbf{k}}}{\partial R_{\kappa\alpha}(\mathbf{q})} \middle| \frac{\partial \hat{H}_{\mathbf{k},\mathbf{k}}}{\partial R_{\kappa'\gamma}(\mathbf{q})} \middle| u^{(0)}_{n\mathbf{k}} \right\rangle, \tag{14}$$

where the summation over energetic bands (above M) has been replaced by the solution $|\hat{P}_{c\mathbf{k}+\mathbf{q}} \frac{\partial u_{n\mathbf{k}}}{\partial R_{\kappa\alpha}(\mathbf{q})}\rangle$ of a linear equation as proposed by Sternheimer[24] and applied to this problem in Ref. 17. The definition for the projector $\hat{P}_{c\mathbf{k}+\mathbf{q}}$ and active space M as well as the description of the linear equation to be solved can be found in the Appendix of Ref. 11.

We finally obtain the adiabatic temperature-dependent renormalization in the RIA by neglecting the non-RIA contribution as defined by Eq. (13), which yields

$$\begin{aligned}
\Delta\varepsilon^{(\mathrm{adiabatic,RIA})}_{n\mathbf{k}}(T) = \Re \frac{1}{N_q} \sum_{\mathbf{q}} \sum_{m}^{3N} \left(n_{m\mathbf{q}}(T) + \frac{1}{2} \right) \frac{1}{4\omega_{m\mathbf{q}}} \sum_{\substack{\kappa\alpha \\ \kappa'\gamma}} \Bigg\{ \Bigg(\Bigg(\Bigg[\sum_{n'=1}^{M}{}' \frac{\left\langle u^{(0)}_{n\mathbf{k}} \middle| \frac{\partial \hat{H}_{\mathbf{k},\mathbf{k}}}{\partial R_{\kappa\alpha}(-\mathbf{q})} \middle| u^{(0)}_{n'\mathbf{k}+\mathbf{q}} \right\rangle \left\langle u^{(0)}_{n'\mathbf{k}+\mathbf{q}} \middle| \frac{\partial \hat{H}_{\mathbf{k},\mathbf{k}}}{\partial R_{\kappa'\gamma}(\mathbf{q})} \middle| u^{(0)}_{n\mathbf{k}} \right\rangle}{\varepsilon^{(0)}_{n\mathbf{k}} - \varepsilon^{(0)}_{n'\mathbf{k}+\mathbf{q}} + i\delta} \\
+ \left\langle \hat{P}_{c\mathbf{k}+\mathbf{q}} \frac{\partial u_{n\mathbf{k}}}{\partial R_{\kappa\alpha}(\mathbf{q})} \middle| \frac{\partial \hat{H}_{\mathbf{k},\mathbf{k}}}{\partial R_{\kappa'\gamma}(\mathbf{q})} \middle| u^{(0)}_{n\mathbf{k}} \right\rangle \Bigg] + (\kappa\alpha) \leftrightarrow (\kappa'\gamma) \Bigg) + (c.c.) \Bigg) U^*_{m,\kappa'\gamma}(\mathbf{q}) U_{m,\kappa\alpha}(\mathbf{q}) \\
- \frac{1}{2} \Bigg(\Bigg(\Bigg[\sum_{n'=1}^{M}{}' \frac{\left\langle u^{(0)}_{n\mathbf{k}} \middle| \frac{\partial \hat{H}_{\mathbf{k},\mathbf{k}}}{\partial R_{\kappa\alpha}(\mathbf{\Gamma})} \middle| u^{(0)}_{n'\mathbf{k}} \right\rangle \left\langle u^{(0)}_{n'\mathbf{k}} \middle| \frac{\partial \hat{H}_{\mathbf{k},\mathbf{k}}}{\partial R_{\kappa'\gamma}(\mathbf{\Gamma})} \middle| u^{(0)}_{n\mathbf{k}} \right\rangle}{\varepsilon^{(0)}_{n\mathbf{k}} - \varepsilon^{(0)}_{n'\mathbf{k}} + i\delta} + \left\langle \hat{P}_{c\mathbf{k}} \frac{\partial u_{n\mathbf{k}}}{\partial R_{\kappa\alpha}(\mathbf{\Gamma})} \middle| \frac{\partial \hat{H}_{\mathbf{k},\mathbf{k}}}{\partial R_{\kappa'\gamma}(\mathbf{\Gamma})} \middle| u^{(0)}_{n\mathbf{k}} \right\rangle \Bigg] \\
+ (\kappa\alpha) \leftrightarrow (\kappa'\gamma) \Bigg) + (c.c.) \Bigg) \left(U^*_{m,\kappa\gamma}(\mathbf{q}) U_{m,\kappa\alpha}(\mathbf{q}) + U^*_{m,\kappa'\gamma}(\mathbf{q}) U_{m,\kappa'\alpha}(\mathbf{q}) \right) \Bigg\},
\end{aligned} \tag{15}$$

where a small imaginary component $i\delta$ is usually introduced in the AHC equation to smooth the energy denominators. For example, in the case of diamond, several authors have used an $i\delta$ of 100 meV to account for the finite lifetimes of the electronic states.[8,9,16,25] However, the theory must also be valid (apart from controlled numerical instabilities) for vanishing $i\delta$. This point will be further discussed in Section III.

B. Beyond the Rayleigh-Schrödinger perturbation theory

Phonons affect the one-electron energy bands $\varepsilon_{n\mathbf{k}}$ in two ways: there is a shift $\Delta\varepsilon_{n\mathbf{k}}$ and a lifetime broadening $1/\tau_{n\mathbf{k}}$. As seen in Subsection II A, the adiabatic approximation leads to a real renormalization of the eigenstates (and no broadening). Thus, the study of the lifetime broadening requires an extension of the adiabatic theory.

In 1978, Allen generalized his earlier work,[12] derived within the standard Rayleigh-Schrödinger perturbation theory, using MBP techniques to include finite phonon frequencies.[26] These techniques describe excitations in terms of spectral functions,[19,27] where quasiparticles cannot always be unambiguously identified with the associated well defined eigenenergies. We will refer to this technique as the dynamical AHC theory, which goes beyond the Born-Oppenheimer approximation. We obtain the following equation, which contains the electron-phonon matrix elements already calculated for the adiabatic renormalization:

$$\begin{aligned}\Delta\varepsilon_{n\mathbf{k}}^{(\text{dynamic,RIA})}(T,\omega) = \Re\frac{1}{N_q}\sum_{\mathbf{q}}\sum_{m}^{3N}\frac{1}{4\omega_{m\mathbf{q}}}\sum_{\substack{\kappa\alpha\\ \kappa'\gamma}}\Bigg\{\Bigg(\Bigg(\Bigg[\sum_{n'=1}^{M}\Big\langle u_{n\mathbf{k}}^{(0)}\Big|\frac{\partial\hat{H}_{\mathbf{k},\mathbf{k}}}{\partial R_{\kappa\alpha}(-\mathbf{q})}\Big|u_{n'\mathbf{k}+\mathbf{q}}^{(0)}\Big\rangle\Big\langle u_{n'\mathbf{k}+\mathbf{q}}^{(0)}\Big|\frac{\partial\hat{H}_{\mathbf{k},\mathbf{k}}}{\partial R_{\kappa'\gamma}(\mathbf{q})}\Big|u_{n\mathbf{k}}^{(0)}\Big\rangle\\ \times\frac{1}{2}\Big(\frac{n_{m\mathbf{q}}(T)+f_{n'\mathbf{k}+\mathbf{q}}}{\omega-\varepsilon_{n'\mathbf{k}+\mathbf{q}}^{(0)}+\omega_{m\mathbf{q}}+i\eta+i\delta}+\frac{n_{m\mathbf{q}}(T)+1-f_{n'\mathbf{k}+\mathbf{q}}}{\omega-\varepsilon_{n'\mathbf{k}+\mathbf{q}}^{(0)}-\omega_{m\mathbf{q}}+i\eta+i\delta}\Big)\\ +\Big\langle P_{c\mathbf{k}+\mathbf{q}}\frac{\partial u_{n\mathbf{k}}}{\partial R_{\kappa\alpha}(\mathbf{q})}\Big|\frac{\partial\hat{H}_{\mathbf{k},\mathbf{k}}}{\partial R_{\kappa'\gamma}(\mathbf{q})}\Big|u_{n\mathbf{k}}^{(0)}\Big\rangle\Big(n_{m\mathbf{q}}(T)+\frac{1}{2}\Big)\Big]+(\kappa\alpha)\leftrightarrow(\kappa'\gamma)\Big)+(c.c.)\Bigg)U_{m,\kappa'\gamma}^{*}(\mathbf{q})U_{m,\kappa\alpha}(\mathbf{q})\\ -\frac{1}{2}\Bigg(\Bigg(\Bigg[\sum_{n'=1}^{M}\frac{\big\langle u_{n\mathbf{k}}^{(0)}\big|\frac{\partial\hat{H}_{\mathbf{k},\mathbf{k}}}{\partial R_{\kappa\alpha}(\mathbf{\Gamma})}\big|u_{n'\mathbf{k}}^{(0)}\big\rangle\big\langle u_{n'\mathbf{k}}^{(0)}\big|\frac{\partial\hat{H}_{\mathbf{k},\mathbf{k}}}{\partial R_{\kappa'\gamma}(\mathbf{\Gamma})}\big|u_{n\mathbf{k}}^{(0)}\big\rangle}{\omega-\varepsilon_{n'\mathbf{k}}^{(0)}+i\delta}+\Big\langle P_{c\mathbf{k}}\frac{\partial u_{n\mathbf{k}}}{\partial R_{\kappa\alpha}(\mathbf{\Gamma})}\Big|\frac{\partial\hat{H}_{\mathbf{k},\mathbf{k}}}{\partial R_{\kappa'\gamma}(\mathbf{\Gamma})}\Big|u_{n\mathbf{k}}^{(0)}\Big\rangle\Bigg]\\ +(\kappa\alpha)\leftrightarrow(\kappa'\gamma)\Big)+(c.c.)\Bigg)\Big(n_{m\mathbf{q}}(T)+\frac{1}{2}\Big)\Big(U_{m,\kappa\gamma}^{*}(\mathbf{q})U_{m,\kappa\alpha}(\mathbf{q})+U_{m,\kappa'\gamma}^{*}(\mathbf{q})U_{m,\kappa'\alpha}(\mathbf{q})\Big)\Bigg\},\end{aligned}\tag{16}$$

where $f_{n\mathbf{k}}$ is the electronic occupation of the wavevector $\mathbf{k}$ at band n, where a convergence study on M is required for the Fan term due to the fact that the Sternheimer solution neglects the phonon frequency $\omega_{m\mathbf{q}}$, while the sum over the active space does not, where $i\eta$ is the mathematical (as opposed to the numerical nature of $i\delta$) infinitesimal shift of the poles $\varepsilon_{n'\mathbf{k}+\mathbf{q}}^{(0)}-\omega_{m\mathbf{q}}$ to the lower part of the complex plane, which is required to enforce causality in MBPT, and where $(c.c.)$ stands for the complex conjugate of the previous term, except for $i\eta$, whose sign must not be changed in the complex conjugation.

In this work, following Allen,[26] rather than obtaining the full spectral function to describe the electronic excitation, we suppose that their description in terms of quasiparticles is still valid and evaluate the associated eigenenergies by correcting the DFT eigenvalues to first-order in perturbation theory, taking the self-energy evaluated at $\omega=\varepsilon_{n\mathbf{k}}^{(0)}$ as the perturbation. Complex eigenenergies are obtained within this generalization that we refer to as the non-adiabatic AHC theory,[26,28]

$$\Delta\varepsilon_{n\mathbf{k}}^{(\text{non-adiabatic,RIA})}(T)=\Delta\varepsilon_{n\mathbf{k}}^{(\text{dynamic,RIA})}(T,\omega=\varepsilon_{n\mathbf{k}}^{(0)}).\tag{17}$$

The phonon-induced lifetime broadening $1/\tau_{n\mathbf{k}}$ is the imaginary part of Eq. (16) with $\omega=\varepsilon_{n\mathbf{k}}^{(0)}$ and $i\delta=0$ (i.e., $1/\tau_{n\mathbf{k}}$ stems from the infinitesimal shift $i\eta$ introduced by MBPT),

$$\begin{aligned}\frac{1}{2\tau_{n\mathbf{k}}^{(\text{non-adiabatic,RIA})}}&=\frac{\pi}{N_q}\sum_{\mathbf{q}}\sum_{m}^{3N}\frac{1}{8\omega_{m\mathbf{q}}}\sum_{\substack{\kappa\alpha\\ \kappa'\gamma}}U_{m,\kappa'\gamma}^{*}(\mathbf{q})U_{m,\kappa\alpha}(\mathbf{q})\sum_{n'=1}^{M}{}'\\ &\times\Bigg(\Big[\Big[\Big\langle u_{n\mathbf{k}}^{(0)}\Big|\frac{\partial\hat{H}_{\mathbf{k},\mathbf{k}}}{\partial R_{\kappa\alpha}(-\mathbf{q})}\Big|u_{n'\mathbf{k}+\mathbf{q}}^{(0)}\Big\rangle\Big\langle u_{n'\mathbf{k}+\mathbf{q}}^{(0)}\Big|\frac{\partial\hat{H}_{\mathbf{k},\mathbf{k}}}{\partial R_{\kappa'\gamma}(\mathbf{q})}\Big|u_{n\mathbf{k}}^{(0)}\Big\rangle\Big]\\ &+(\kappa\alpha)\leftrightarrow(\kappa'\gamma)\Big]+(c.c.)\Bigg)\\ &\times\Big(\big(n_{m\mathbf{q}}(T)+f_{n'\mathbf{k}+\mathbf{q}}\big)\delta(\varepsilon_{n\mathbf{k}}^{(0)}-\varepsilon_{n'\mathbf{k}+\mathbf{q}}^{(0)}+\omega_{m\mathbf{q}})\\ &+\big(n_{m\mathbf{q}}(T)+1-f_{n'\mathbf{k}+\mathbf{q}}\big)\delta(\varepsilon_{n\mathbf{k}}^{(0)}-\varepsilon_{n'\mathbf{k}+\mathbf{q}}^{(0)}-\omega_{m\mathbf{q}})\Big),\end{aligned}\tag{18}$$

where δ is the Dirac delta (which we broaden for numerical reasons).

The phonon-induced lifetime broadening in the adiabatic limit ($\omega_{m\mathbf{q}}<<\varepsilon_{n\mathbf{k}}^{(0)}-\varepsilon_{n'\mathbf{k}+\mathbf{q}}^{(0)}$) is

$$\begin{aligned}\frac{1}{2\tau_{n\mathbf{k}}^{(\text{adiabatic,RIA})}}=\frac{\pi}{N_q}\sum_{\mathbf{q}}\sum_{m}^{3N}\frac{1}{4\omega_{m\mathbf{q}}}\Big(n_{m\mathbf{q}}(T)+\frac{1}{2}\Big)\sum_{\substack{\kappa\alpha\\ \kappa'\gamma}}\sum_{n'=1}^{M}{}'\Bigg(\Big[\Big[\Big\langle u_{n\mathbf{k}}^{(0)}\Big|\frac{\partial\hat{H}_{\mathbf{k},\mathbf{k}}}{\partial R_{\kappa\alpha}(-\mathbf{q})}\Big|u_{n'\mathbf{k}+\mathbf{q}}^{(0)}\Big\rangle\\ \times\Big\langle u_{n'\mathbf{k}+\mathbf{q}}^{(0)}\Big|\frac{\partial\hat{H}_{\mathbf{k},\mathbf{k}}}{\partial R_{\kappa'\gamma}(\mathbf{q})}\Big|u_{n\mathbf{k}}^{(0)}\Big\rangle\Big]+(\kappa\alpha)\leftrightarrow(\kappa'\gamma)\Big]+(c.c.)\Bigg)\delta(\varepsilon_{n\mathbf{k}}^{(0)}-\varepsilon_{n'\mathbf{k}+\mathbf{q}}^{(0)})U_{m,\kappa'\gamma}^{*}(\mathbf{q})U_{m,\kappa\alpha}(\mathbf{q}).\end{aligned}\tag{19}$$

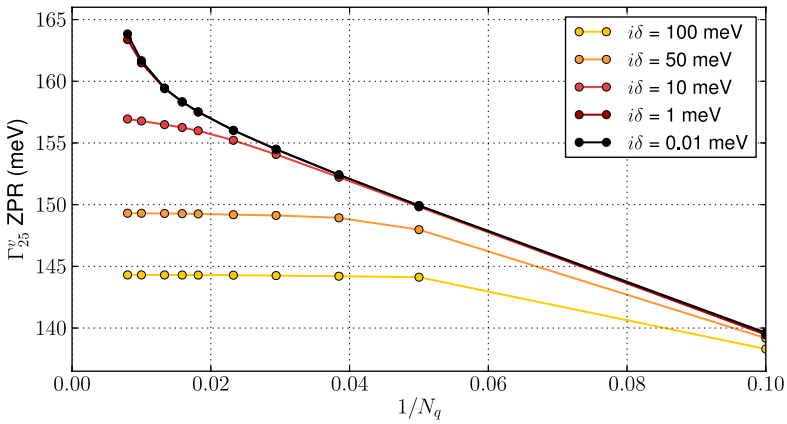

FIG. 1. Adiabatic ZPR of the Γ^v_{25} state of diamond with respect to the **q**-point grid density for decreasing values of $i\delta$ before restoration of the charge neutrality. The size of the **q**-point grid is $N_q \times N_q \times N_q$.

The adiabatic and non-adiabatic renormalizations, Eqs. (15) and (17), as well as adiabatic lifetime Eq. (19) have been coded in the ABINIT software (v7.11) and will be used in Sections III–VI.

III. PHONON WAVEVECTOR SAMPLING AND THE DIVERGENCE PROBLEM

A. Potential breakdown of perturbation theory

Quantum mechanical perturbation theory can breakdown when vanishing denominators appear in the perturbation series. This can happen in the present case, as the short-hand form of Eq. (15) is

$$\Delta\varepsilon_{n\mathbf{k}}^{(\text{adiabatic,RIA})}(T) \propto \sum_{\mathbf{q}} \frac{|GKK(\mathbf{q})|^2}{\varepsilon^{(0)}_{\mathbf{k}} - \varepsilon^{(0)}_{\mathbf{k+q}}}. \tag{20}$$

Actually, there are two types of potential divergences in Eq. (20): (i) when $\varepsilon^{(0)}_{\mathbf{k}} = \varepsilon^{(0)}_{\mathbf{k+q}}$ and (ii) when the electron-phonon matrix elements $GKK(\mathbf{q})$ diverge, which happens when the Born effective charges do not vanish, as we shall see ($GKK(\mathbf{q})$ is then proportional to $\frac{1}{\mathbf{q}}$).

In practical calculations, the $\mathbf{q} = \mathbf{0}$ contribution from the same band (the denominator being thus zero) is not included in the summation. Also, in case of degeneracies, the terms with zero denominators are ignored. However, a large sampling density of **q**-points are needed to include correctly the contributions of the poles of the function. For this reason, the numerical convergence of the adiabatic ZPR of diamond with respect to **q**-point density is slow and requires large **q**-point grids.[16] This problem is often assessed in practice by adding an *ad hoc* $i\delta$ to the denominator of Eq. (20).

IR-active materials exhibit non-zero Born effective charges, which describe the coupling between the electric field generated by the dipoles present in these materials and the ionic motion. Those dipoles, as mentioned previously, also lead to IR active phonon modes. In these cases, the non-zero oscillator strengths (see Eq. (54) of Ref. 29) associated to these modes cause a divergence in the $GKK(\mathbf{q})$. Divergences of type (ii) are therefore present in these materials. However, in IR-inactive materials, there are theoretically no such effective charges and there should therefore be no divergence of type (ii). Since divergences of type (i) have a finite integral when no divergences of type (ii) are present, the **q**-point sum should converge to a finite value for IR-inactive materials. Following the work of Zallen *et al.*,[30] among the non-metallic materials, the only IR-inactive ones are those with only one type of atom and no more than two atoms per unit cell except for the two exceptional space groups $P6/mmm$ and $P6_3/mmc$ where materials with one type of atom but four atoms per unit cell can be found to be also IR-inactive.

In practice, however, we observe a non-physical divergence of the ZPR for large **q**-points densities, even in IR-inactive materials. This effect can be clearly seen in Figure 1, where the **q**-point density dependence of the adiabatic Γ^v_{25} ZPR of diamond (calculated using Eq. (15)) for vanishing $i\delta$ exhibits a divergent behavior when δ is 1 meV or 0.01 meV (hardly seen for δ equal to 50 meV or 100 meV), despite its lack of IR activity.

Actually, this divergence is attributed to a residual electric field stemming from the breaking of the Born effective charge neutrality sum rule in IR-inactive periodic solids. This leads to the presence of divergences of type (ii) which, combined to these of type (i), cause the integral around $\mathbf{q} = \mathbf{0}$ (and the associated **q**-point sum) to diverge.

This residual electric field stems from the finite **k**-point grid used within DFT. Indeed, the first-order density is obtained thanks to a discretized integral on the BZ (see Eq. (B9) of Ref. 31). This first-order density in turn determines the electric field and the Born effective charges (see Eq. (42) of Ref. 29). This residual electric field is found to converge to zero exponentially but is nonetheless substantial at **k**-point grid usually sufficient to converge other relevant quantities. An example of this slow convergence is given in Table I for the case of diamond.

TABLE I. Born effective charge of one carbon atom in diamond, for different electronic wavevector samplings. Since diamond is IR-inactive, the charge should physically be zero, but a very slow convergence with the sampling is found in practice.

Number of **k**-points	Born effective charge
8	−2.5406
64	−0.3514
216	−0.0534
512	−0.0080
1000	−0.0011

B. Restoration of the charge neutrality

In this section, we present a scheme to numerically remove this spurious electric field and thus considerably speed up the ZPR convergence with respect to the electronic wavevector sampling. To this end, let us study the impact of a small Born effective charge on the matrix elements of $\frac{\partial \hat{H}_{\mathbf{k},\mathbf{k}}}{\partial R_{\kappa\alpha}(\mathbf{q})}$ present in Eq. (15). We introduce the following short-hand notation for derivatives, which matches the one used in Ref. 31:

$$\frac{\partial \hat{H}_{\mathbf{k},\mathbf{k}}}{\partial R_{\kappa\alpha}(\mathbf{q})} \triangleq H^{(1)}_{\mathbf{k}+\mathbf{q},\mathbf{k}}. \tag{21}$$

As mentioned in Ref. 31, Eq. (61), within the pseudopotential framework, $H^{(1)}_{\mathbf{q}}$ can be decomposed into a first-order change of the separable, local, Hartree and exchange-correlation potentials,

$$H^{(1)}_{\mathbf{k}+\mathbf{q},\mathbf{k}} = v^{(1)}_{sep,\mathbf{k}+\mathbf{q},\mathbf{k}} + \bar{v}^{(1)}_{loc,\mathbf{q}} + \bar{v}^{(1)}_{H,\mathbf{q}} + \bar{v}^{(1)}_{xc,\mathbf{q}}, \tag{22}$$

where the bar symbol above a quantity $\bar{X}$ means that it is the periodic part of X,

$$\bar{X}^{(1)}_{\mathbf{q}}(\mathbf{r}) = e^{-i\mathbf{q}\cdot\mathbf{r}} X^{(1)}_{\mathbf{q}}(\mathbf{r}), \tag{23}$$

and where both $\bar{v}^{(1)}_{loc,\mathbf{q}}$ and $\bar{v}^{(1)}_{H,\mathbf{q}}$ diverge as $\frac{1}{|\mathbf{q}|}$ with opposite signs.

To make this more explicit, we express $\bar{v}^{(1)}_{loc,\mathbf{q}}$ as (see Eq. (50) of Ref. 31)

$$\bar{v}^{(1)}_{loc,\mathbf{q}}(\mathbf{G}) = \frac{-i}{\Omega_0}(\mathbf{G}+\mathbf{q})_\alpha e^{-i(\mathbf{G}+\mathbf{q})\cdot\boldsymbol{\tau}_\kappa} v^{loc}_\kappa(\mathbf{G}+\mathbf{q}), \tag{24}$$

where Ω_0 is the volume of the unperturbed unit cell, $\boldsymbol{\tau}_\kappa$ the vector position of the atom κ in the unit cell and with (see Eq. (A17) of Ref. 31)

$$v^{loc}_\kappa(\mathbf{q}\to 0) = -\frac{4\pi Z_\kappa}{q^2} + C_\kappa + O(q^2), \tag{25}$$

where Z_κ is the number of valence electrons of the atom κ described in the pseudopotential. To explicit the same behavior in $\bar{v}^{(1)}_{H,\mathbf{q}}$, we express it as (see Eq. (62) of Ref. 31)

$$\bar{v}^{(1)}_{H,\mathbf{q}}(\mathbf{G}) = 4\pi \frac{\bar{n}^{(1)}_{\mathbf{q}}}{|\mathbf{G}+\mathbf{q}|^2}. \tag{26}$$

Since $\bar{v}^{(1)}_{loc,\mathbf{q}}(\mathbf{G})$ in Eq. (24) has an analytic expression for $\mathbf{q}\to 0$, a residual electric charge can only affect the first-order density $\bar{n}^{(1)}_{\mathbf{q}}$ in Eq. (26). The derivation of the impact of a residual Born effective charge on the first-order density is presented in Appendix A of this paper and can be seen in Eq. (A77) in the $\mathbf{G}=\mathbf{0}$ limit. For practical reasons, we apply the renormalization to any $\mathbf{G}$ as it will converge to the same result when the $\mathbf{k}$-point grid is large enough.

Using this knowledge, we can renormalize the Hartree term as follows (see Eq. (A81)):

$$\bar{v}^{ren(1)}_{H,\mathbf{q}}(\mathbf{G}) = \bar{v}^{(1)}_{H,\mathbf{q}}(\mathbf{G}) \frac{\sum_\gamma q_\gamma \left(Z_\kappa \delta_{\alpha\gamma} - \frac{(Z^*_{\kappa\alpha,\gamma} - \bar{Z}_{\alpha\gamma})}{\frac{1}{q^2}\sum_{\delta,\xi} q_\delta \epsilon_{\delta\xi} q_\xi} \right)}{\sum_\gamma q_\gamma \left(Z_\kappa \delta_{\alpha\gamma} - \frac{Z^*_{\kappa\alpha,\gamma}}{\frac{1}{q^2}\sum_{\delta,\xi} q_\delta \epsilon_{\delta\xi} q_\xi} \right)}, \tag{27}$$

where $Z^*_{\kappa,\alpha\beta}$ is the Born effective charge, $\epsilon_{\gamma\xi}$ is the macroscopic static dielectric tensor for the electronic system (where the ions are considered fixed), and $\bar{Z}_{\alpha\beta}$ is the averaged Born effective charge

$$\bar{Z}_{\alpha\beta} = \frac{1}{N_{at}} \sum_\kappa Z^*_{\kappa,\alpha\beta}, \tag{28}$$

where N_{at} is the number of atoms in the primitive cell. If the Born effective charge neutrality sum rule was fulfilled, $\bar{Z}_{\alpha\beta}$ should be exactly zero.

With this renormalization, the $\bar{v}^{ren(1)}_{H,\mathbf{q}}$ term correctly cancels the $\bar{v}^{(1)}_{loc,\mathbf{q}}$ when $\mathbf{q}\to 0$. Figure 2 shows the faster convergence rate of the ZPR with respect to the density of the $\mathbf{k}$-point grid obtained with this renormalization for the specific case of the first band of diamond at $\mathbf{k}=\mathbf{L}$. To highlight the divergent behavior of the ZPR with respect to $\mathbf{q}$-point grid density without the associated high computational cost for $\mathbf{q}$-point integration, only 6 symmetry equivalent $\mathbf{q}$-points are used in the sum. The $\mathbf{q}$-points are chosen close enough to zero to show the divergence, $\mathbf{q} = \frac{1}{100}\mathbf{X}$.

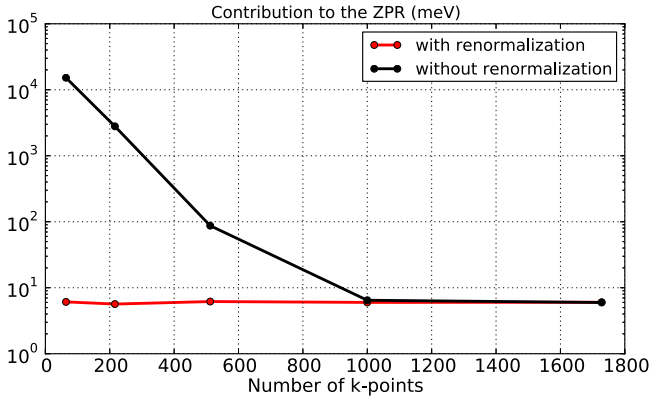

FIG. 2. Contribution to the ZPR of 6 $\mathbf{q}$-points with respect to the densification of the $\mathbf{k}$-point grid of the first band of diamond at $\mathbf{k}=\mathbf{L}$. Only 6 symmetry equivalent $\frac{1}{100}\mathbf{X}$ $\mathbf{q}$-points are used. The calculations were done with and without the renormalization of Eq. (27).

IV. BEHAVIOR OF THE q-POINT CONVERGENCE

After enforcing the charge neutrality by application of Eq. (27), the theoretical rate of convergence of the ZPR can be analyzed when the number of $\mathbf{q}$-points along a side of the Brillouin Zone N_q increases (the total number of $\mathbf{q}$-points in the Brillouin Zone being N_q^3). Thus, in this section, we first isolate the divergent contribution to the ZPR and then study analytically its convergence rate.

This study reveals that the $\mathbf{q}$-point convergence can be either constant, linear ($1/N_q$), or divergent (N_q) depending on the state that is renormalized, depending on the use of the adiabatic (Eq. (15)) or non-adiabatic (Eq. (17)) equation as well as depending on the IR activity of the material. Table II gives a summary of those behaviors.

A. Rapid convergence with N_q

1. IR-inactive materials in the non-adiabatic approximation at VBM/CBM

For an IR-inactive material within the non-adiabatic approximation (Eq. (17)), we can model the $\mathbf{q}$-point behavior of

TABLE II. Convergence behavior of the renormalized eigenstates with the densification of the **q**-grid. The only case where the renormalization diverges is for an IR-active material at the VMB/CBM when the adiabatic approximation is used. The referenced subsections are given in parentheses.

Cases		q-convergence	
		Adiabatic	Non-adiabatic
IR-inactive	VBM/CBM	$1/N_q$ (IV B 1)	Flat (IV A 1)
	Other	Flat (IV A 2)	Flat (IV A 2)
IR-active	VBM/CBM	N_q (IV C)	$1/N_q$ (IV B 2)
	Other	$1/N_q$ (IV B 2)	$1/N_q$ (IV B 2)

the ZPR of the valence band maximum (VBM) with

$$\lim_{\delta\to 0}\iiint_0^{q_c} d^3q \frac{1}{\varepsilon_{n\mathbf{k}} - \varepsilon_{n'\mathbf{k+q}} + \omega_{\mathbf{q}} + i\delta}, \tag{29}$$

where q is integrated in a sphere of radius q_c around Γ. The same derivation applies for the conduction band minimum (CBM) with $-\omega_{\mathbf{q}}$, the energy difference $\varepsilon_{n\mathbf{k}} - \varepsilon_{n\mathbf{k+q}}$ being negative. The phonon frequency shifts the poles of the function, so that the integrand is analytic over the domain of integration. The parabolic ($\propto q^2$) behavior of the extrema leads from Eq. (29) to

$$= \lim_{\delta\to 0}\iiint_0^{q_c} d^3q \frac{1}{q^2 + \omega + i\delta} \tag{30}$$

$$= \lim_{\delta\to 0}\int_0^{q_c} dq \int_{-\pi}^{\pi} d\phi \int_0^{\pi} d\theta \frac{q^2 \sin\theta}{q^2 + \omega + i\delta} \tag{31}$$

$$= \int_0^{q_c} dq 4\pi \frac{q^2}{q^2 + \omega} \tag{32}$$

$$= 4\pi\sqrt{\omega}\Big(\frac{q_c}{\sqrt{\omega}} - \tan^{-1}\Big(\frac{q_c}{\sqrt{\omega}}\Big)\Big). \tag{33}$$

A Taylor expansion around $q_c = 0$ reveals that

$$4\pi\sqrt{\omega}\Big(\frac{q_c}{\sqrt{\omega}} - \tan^{-1}\Big(\frac{q_c}{\sqrt{\omega}}\Big)\Big) = \frac{4\pi\sqrt{\omega}}{3}\Big(\frac{q_c}{\sqrt{\omega}}\Big)^3 + O(q_c^5), \tag{34}$$

which means that the contribution from the integration around $q = 0$ is simply proportional to the volume of integration, as expected given the non-divergent nature of the integrand.

Thus, neglecting the $q = 0$ contribution in the **q**-point sum of the non-adiabatic ZPR for a band extrema of an IR-inactive material causes an error proportional to $\frac{1}{N_q^3}$, whereas discretization of the **q**-point integration over the BZ with the rectangle method causes an error proportional to $\frac{1}{N_q^2}$. Therefore, the error caused by the neglected $q = 0$ contribution is not visible in the global convergence behavior for this ZPR. This behavior will thus be referred to as "flat" convergence with respect to **q**-point grid density from now on.

Additionally, we can numerically integrate Eq. (29) on a three dimensional grid of **q**-points using

$$\frac{V}{N_q^3}\sum_{q}\frac{1}{q^2 + \omega + i\delta}, \tag{35}$$

where V is the volume of integration and where the element of volume is inversely proportional to the number of **q**-points N_q^3 needed to discretize the grid. An example of the convergence

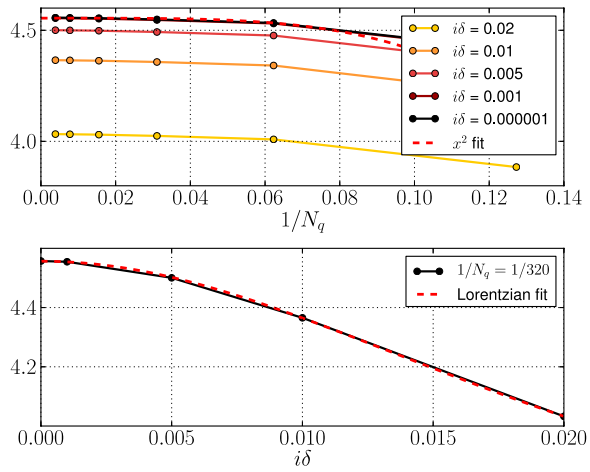

FIG. 3. Behavior of the numerical integral of Eq. (35) with respect to the **q**-point density and δ for $q_c = 0.5$ and $\omega = 0.01$.

of Eq. (35) with $\frac{1}{N_q}$ is shown on the top of Figure 3 for $q_c = 0.5$ and $\omega = 0.01$.

This function converges very quickly with increasing **q**-sampling, which can also be seen on a real material like the VBM of diamond (see the center of Figure 7(a)).

2. IR-inactive materials in the adiabatic or non-adiabatic approximation for a non-extremal eigenvalue

If the state that we would like to renormalize is not a VBM nor a CBM, the denominator of the adiabatic (Eq. (15)) or non-adiabatic (Eq. (17)) equations will be small when the state that we consider ($\varepsilon_{n\mathbf{k}}$) has almost the same energy as another state ($\varepsilon_{n'\mathbf{k+q}}$) (in the adiabatic case) or as another state minus a phonon frequency ($\varepsilon_{n'\mathbf{k+q}} - \omega_{m\mathbf{q}}$) (in the non-adiabatic case). As a result, the integrand in Eq. (29) is not analytic anymore in these cases and a non-zero imaginary $i\delta$ is required to avoid numerical instabilities.

To study analytically the adiabatic case, we will model the energy difference ($\varepsilon_{n\mathbf{k}} - \varepsilon_{n'\mathbf{k+q}}$) by a shifted parabola with its minimum at $\mathbf{q}_0$,

$$\varepsilon_{\mathbf{k}} - \varepsilon_{\mathbf{k+q}} = (\mathbf{q} - \mathbf{q}_0)^2 - q_0^2. \tag{36}$$

The ZPR has poles on a sphere of radius q_0 centered on $\mathbf{q} = \mathbf{q_0}$ (chosen to be on the z-axis) and passing through the origin. The integral on the spherical shell between radii of values $q_0 - \Delta$ and $q_0 + \Delta$ gives a contribution that is linear with Δ (see Appendix B 1), as would any regular function when integrated over a spherical shell. This indicates that the integration of these poles will not contribute an error of higher order than the remainder of the numerical integration. Moreover, neglecting the $\mathbf{q} = 0$ contribution in the numerical integration yields an error proportional to $\frac{1}{N_q^3}$ in the IR-inactive case (see Appendix B 2). Thus, these two numerical issues lead to a **q**-point grid convergence that is flat for a non-extremal eigenenergy of an IR-inactive material in the adiabatic framework.

In the non-adiabatic case, the ω to be added to the right-hand side of Eq. (36) only slightly reduces the radius of the sphere at $\mathbf{q}_0$ (which thus does not touch the origin anymore)

and the conclusion for the adiabatic case remains valid for the numerical integration over this shell, i.e., it does not contribute an error of higher order than the remainder of the numerical integration. Also, the integrand at $\mathbf{q} = \mathbf{0}$ is analytical in the non-adiabatic case, so that only the first issue of the adiabatic case persists in the non-adiabatic one, which leaves the convergence behavior flat.

Therefore, in the present cases, the $\mathbf{q}$-point integration required to evaluate the ZPR converges just as well as if there was no divergence issues in the integrand, so that no special extrapolation is required. An example of this type of convergence is given at the top of Figure 6(a) for diamond in the adiabatic framework at a non-extremal energy.

Note that this well-behaved convergence behavior is particular to non-extremal eigenenergies for IR-inactive materials in the adiabatic framework as well as any eigenvalue for IR-inactive materials in the non-adiabatic framework. In other cases, the discretized integral does not converge as quickly as the rectangle method for an analytical integrand. It sometimes converges linearly ($\propto \frac{1}{N_q}$) (see Subsection IV B) or even diverges ($\propto N_q$) (see Subsection IV C).

B. Convergence proportional to the inverse of N_q

1. IR-inactive materials in the adiabatic approximation at the VBM/CBM

IR-inactive materials with a parabolic energy dispersion (VBM or CBM) have a $\mathbf{q}$-dependence for the adiabatic ZPR that behaves as

$$\iiint_0^{q_c} d^3q \frac{1}{q^2 + i\delta} = 4\pi q_c \propto \frac{1}{N_q}, \tag{37}$$

when $i\delta = 0$. Therefore, neglecting the $q = 0$ contribution in the numerical integration yields an error proportional to $\frac{1}{N_q}$ that dominates the $\frac{1}{N_q^2}$ error of the rectangle method.

The rate of convergence with $\mathbf{q}$-densification can be numerically tested by summing this function on a three dimensional grid of $\mathbf{q}$-points

$$\frac{1}{N_q^3} \sum_{q \neq 0} \frac{1}{q^2 + i\delta}, \tag{38}$$

where the $q = 0$ term has been omitted in the sum for numerical reasons (as the expression must stand for vanishing δ). The numerical integral of Eq. (38) is shown in Figure 4 and converges towards 2π for $q_c = 0.5$, as expected. Note that it converges linearly with the densification of the $\mathbf{q}$-point grid for $\delta = 0$.

2. IR-active materials in the adiabatic approximation for non-extremal eigenvalues and in the non-adiabatic approximation for any eigenvalues

In the case of IR-active materials, the GKK behave as $1/q^2$ for small $\mathbf{q}$, even when the Born effective charge neutrality sum rule is enforced with Eq. (27), since non-zero effective charges are physically present in these materials. However, at VBM or CBM, the phonon frequency ω in the non-adiabatic expression (Eq. (17)) shifts the pole inside the bandgap. Therefore, the parabolic eigenenergy dispersion is not problematic anymore. Combining the behavior of the GKK and the eigenenergy denominator yields

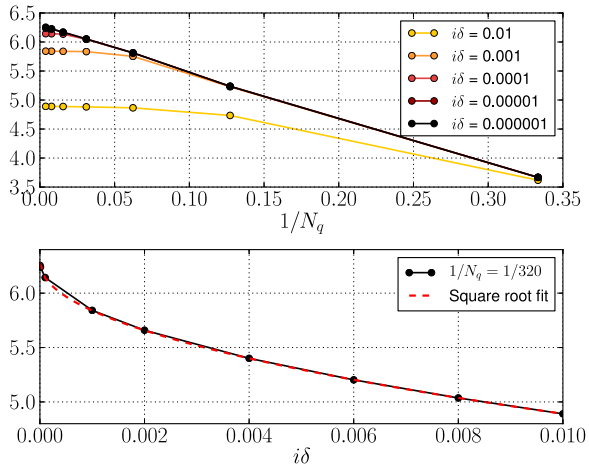

FIG. 4. Behavior of the numerical integration of Eq. (38) with respect to the $\mathbf{q}$-point density and value of $i\delta$ for $q_c = 0.5$.

$$\Re \iiint_0^{q_c} d^3q \frac{1}{q^2(\omega + i\delta)}. \tag{39}$$

This case behaves the same way as Eq. (38). We thus obtain the same linear behavior.

In the case of eigenvalues that are not at VBM or CBM, the $\mathbf{q}$-point integration in the adiabatic and non-adiabatic approximations also exhibits a convergence that is linear with $1/N_q$, as explained at the end of Appendix B 2.

C. Increasing N_q does not lead to convergence (IR-active materials in the adiabatic approximation at the VBM/CBM)

In the case of IR-active materials, when we consider the renormalization of a state at the VBM or the CBM, the adiabatic equation diverges. Indeed,

$$\frac{V}{N_q^3} \sum_q \frac{1}{q^2(q^2 + i\delta)} \tag{40}$$

diverges as N_q. An example of this case is given in the middle left of Figure 5(b) for the VBM of boron nitride (BN) using the adiabatic equation.

More specifically, neglecting the $q = 0$ contribution in the numerical integration of Eq. (40) gives a convergence behavior that can be modeled by the spherical integration of the summand of Eq. (40) in a shell from q_c/N_q to q_c. This gives, for $\delta = 0$,

$$\int_{-\pi}^{\pi} d\phi \int_0^{\pi} d\theta \int_{q_c/N_q}^{q_c} dq \frac{1}{q^4} = 4\pi \int_{q_c/N_q}^{q_c} dq \frac{1}{q^2} = 4\pi \left(\frac{1}{q_c} - \frac{1}{q_c/N_q} \right). \tag{41}$$

As $1/N_q$ goes to 0, the value of this integral indeed diverges linearly with the number of division N_q. This shows that *for IR-active materials, only the non-adiabatic equation can be safely used.*

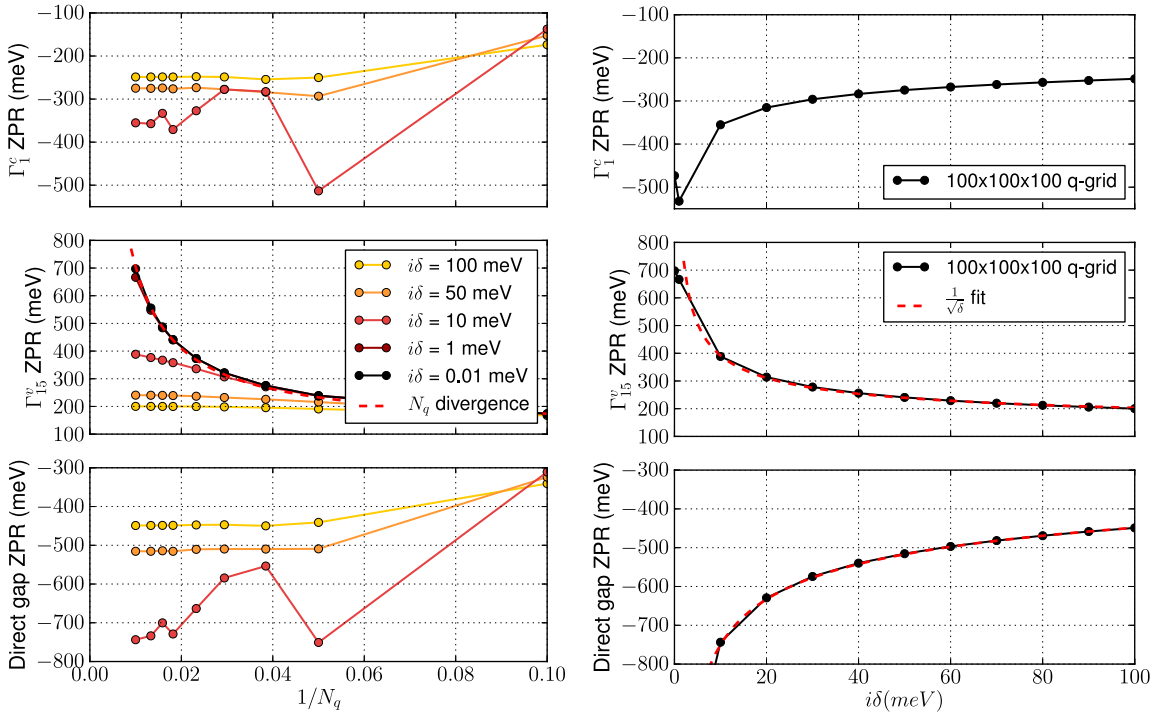

(a) Adiabatic ZPR of c-BN. (b) $i\delta$ extrapolation of the ZPR.

FIG. 5. Convergence study with respect to the (a) **q**-point grid density and (b) $i\delta$ parameter for the adiabatic direct bandgap ZPR of c-BN. The bottom figures are the difference of the two figures above them.

V. BEHAVIOR OF THE *iδ* CONVERGENCES

After enforcing the charge neutrality by application of Eq. (27), the theoretical rate of convergence of the ZPR can be analyzed when the small imaginary parameter $i\delta$ tends to 0. To do so, we proceed in the same way as in Section IV for the **q**-point sampling: we first isolate the divergent contribution to the ZPR and then study analytically its rate of convergence.

This study reveals that the δ convergence can be square-root, linear, or Lorentzian-like, depending on the state that is renormalized, the use of the adiabatic or non-adiabatic framework as well as the IR-activity of the material. Table III gives a summary of those behaviors.

A. Convergence proportional to the square-root of *δ* (IR-inactive material in the adiabatic approximation at the VBM/CBM)

For an IR-inactive material at the VBM or CBM in the adiabatic framework, we can obtain the ZPR dependence on the (finite) δ value by analytically integrating Eq. (37),

$$\Re \iiint d^3q \frac{1}{q^2 + i\delta} = 4\pi \int_0^{q_c} dq \frac{q^4}{q^4 + \delta^2} = 4\pi\sqrt{\delta} \int_0^{q_c} \frac{dq}{\sqrt{\delta}} \frac{\frac{q^4}{\delta^2}}{\frac{q^4}{\delta^2} + 1}. \quad (42)$$

Carrying out the integration and expanding the result around $\frac{\sqrt{\delta}}{q_c} = 0$ yield

$$4\pi q_c + 4\pi C\sqrt{\delta} + O(\delta), \quad (43)$$

where C is a constant. This result matches the $\sqrt{\delta}$ behavior observed in the numerical integration (see Eq. (38)), which is presented at the bottom of Figure 4.

TABLE III. Convergence behavior for $i\delta \to 0$ at converged or extrapolated **q**-point density. The only case where the renormalization diverges is for an IR-active material at the VMB/CBM when the adiabatic approximation is used. The relevant subsections are given in parentheses.

Cases		δ-convergence	
		Adiabatic	Non-adiabatic
IR-inactive	VBM/CBM	$\sqrt{\delta}$ (V A)	Lorentzian (V C 1)
	Other	δ (V B 1)	δ (V B 1)
IR-active	VBM/CBM	$1/\sqrt{\delta}$ (V D)	Lorentzian (V C 2)
	Other	δ (V B 2)	δ (V B 2)

B. Convergence proportional to *δ*

1. *IR-inactive materials in the adiabatic and non-adiabatic approximations at a non-extremal point*

For IR-inactive materials, when considering a **k**-point other than the VBM or CBM, the adiabatic equation can be modeled as

$$\Re \iiint_0^{q_c} d^3q \frac{1}{\varepsilon(\mathbf{q}) + i\delta}, \quad (44)$$

where we have defined $\varepsilon(\mathbf{q}) = \varepsilon_{\mathbf{k}+\mathbf{q}} - \varepsilon_{\mathbf{k}}$.

Since the small $i\delta$ will only affect the integrand around the pole at $\varepsilon(\mathbf{q}) = 0$, we can determine the δ dependence of this model ZPR by considering only a small range of energy η around it. We can then re-write Eq. (44) as

$$\int_{-\eta}^{\eta} dE g(E) f(E), \tag{45}$$

with $g(E) \triangleq \int d^3q \delta(E - \varepsilon(\mathbf{q}))$ the density of states and

$$f(E) \triangleq \frac{1}{E + i\delta}. \tag{46}$$

We can make a Taylor expansion of the density of states around $E = 0$ (since η is small),

$$g(E) = g(0) + g'(0)E + O(E^2). \tag{47}$$

The even terms in Eq. (47) will not contribute to the integral since $\Re f(E)$ is an odd function. Therefore, the leading term is the first-order one. The integral can thus be rewritten as

$$\delta \int_{-\eta}^{\eta} \frac{dE}{\delta} \frac{g'(0)\frac{E^2}{\delta^2}}{\frac{E^2}{\delta^2} + 1} = 2\delta g'(0)\Big(\frac{\eta}{\delta} - \tan^{-1}(\frac{\eta}{\delta})\Big). \tag{48}$$

Expanding Eq. (48) around $\frac{\delta}{\eta} = 0$ yields

$$2g'(0)\eta - \delta g'(0)\pi, \tag{49}$$

which is linear in δ.

In the non-adiabatic framework, the integral changes to

$$\int dE f(E + \omega) g(E). \tag{50}$$

Since this function has poles when $E = -\omega$, we will now integrate around this value

$$\int_{-\omega-\eta}^{-\omega+\eta} dE f(E + \omega) g(E). \tag{51}$$

Substituting $E + \omega \to u$, we obtain

$$\int_{-\eta}^{\eta} du f(u) g(u - \omega). \tag{52}$$

The density of states can again be Taylor expanded around $-\omega$, giving

$$g(u - \omega) = g(-\omega) + ug'(-\omega) + O(u^2). \tag{53}$$

The same steps that led us from Eqs. (47)–(49) now yield

$$2g'(-\omega)\eta - \delta g'(-\omega)\pi, \tag{54}$$

which is again linear in δ.

Thus, whether the adiabatic or the non-adiabatic approximation is used, the behavior of the ZPR of IR-inactive materials for non-extremal eigenvalues is linear when $\delta \to 0$.

2. IR-active materials in the adiabatic and non-adiabatic approximations at a non-extremal point

For IR-active materials at non-extremal eigenvalues, we can use a shifted parabola to model eigenenergy differences (see Eq. (36)) and $\frac{1}{q^2}$ to model the $|GKK|^2$. This yields Eq. (B12) with an extra $\frac{1}{q^2}$ factor in the integrand, which leads to Eq. (B19). From this starting point, the derivations presented in Appendix B 3 show that the ZPR converges linearly with δ in both the adiabatic and the non-adiabatic frameworks. In practice, the value that is reached by the linear regime is very high and tends to infinity at VBM or CBM.

C. δ convergence proportional to a Lorentzian

1. IR-inactive materials in the non-adiabatic approximation at the VBM/CBM

When considering the non-adiabatic framework at the VBM or CBM of an IR-inactive material, the ZPR convergence behavior with respect to δ is

$$\Re \iiint d^3q \frac{1}{q^2 + \omega + i\delta} = 4\pi \Re \int_0^{q_c} dq \frac{q^2}{q^2 + \omega + i\delta}, \tag{55}$$

which yields

$$4\pi \Re\Big(q_c - \sqrt{\omega + i\delta} \tan^{-1}\Big(\frac{q_c}{\sqrt{\omega + i\delta}}\Big)\Big). \tag{56}$$

Plotting Eq. (56) as a function of δ reveals a Lorentzian-like shape centered around $\delta = 0$. This can also be seen in the δ-dependence of the numerical integration of Eq. (55),

$$\frac{1}{N_q^3} \sum_{S_{q_c}} \frac{(q^2 + \omega)}{(q^2 + \omega)^2 + \delta^2}, \tag{57}$$

where S_{q_c} is a sphere of radius q_c. This dependence is shown at the bottom of Figure 3 for a cut-off radius $q_c = 0.5$ and $\omega = 0.01$.

In practice, we also observe that non-adiabatic ZPR for VBM/CBM of IR-inactive materials can be accurately fitted by a Lorentzian function. We thus use this type of function to extrapolate the ZPR at $\delta = 0$.

2. IR-active materials in the non-adiabatic approximation at the VBM/CBM

For IR-active materials, we get an extra $\frac{1}{q^2}$ factor in the integrand of Eq. (55), which thus becomes

$$\begin{aligned} \Re \iiint d^3q \frac{1}{q^2} \frac{1}{q^2 + \omega + i\delta} &= 4\pi \Re \int_0^{\infty} dq \frac{1}{q^2 + \omega + i\delta} \\ &= 2\pi \Re \int_{-\infty}^{\infty} dq \frac{1}{q^2 + \omega + i\delta}. \end{aligned} \tag{58}$$

This integral can be performed by closing the contour of integration using a half-circle of infinite radius in the upper complex plane (which does not contribute to the integral) and then using the residue theorem. We obtain

$$\begin{aligned} 2\pi \Re \int_{-\infty}^{\infty} dq \frac{1}{q^2 + \omega + i\delta} &= 2\pi^2 \frac{1}{\sqrt{\omega}\big(1 + (\frac{\delta}{\omega})^2\big)^{\frac{1}{4}}} \Re e^{-\frac{i}{2}\tan^{-1}(\frac{\delta}{\omega})} \\ &= 2\pi^2 \frac{1}{\sqrt{\omega}\big(1 + (\frac{\delta}{\omega})^2\big)^{\frac{1}{4}}} \cos\Big(\frac{1}{2}\tan^{-1}\Big(\frac{\delta}{\omega}\Big)\Big). \end{aligned} \tag{59}$$

Plotting Eq. (59) reveals a Lorentzian-like shape centered around $\delta = 0$. Accordingly, fitting the results using a Lorentzian is also found to be a good approximation in practice for IR-active materials.

D. Decreasing δ does not lead to convergence

The adiabatic ZPR for the VBM/CBM of an IR-active material has already been shown to diverge with increasing $\mathbf{q}$-point sampling (see Subsection IV C). We now examine the

δ-dependence of the ZPR, which has the form

$$\Re \iiint d^3q \frac{1}{q^2(q^2+i\delta)} = 4\pi \Re \int_0^{q_c} dq \frac{1}{q^2+i\delta} = \frac{4\pi}{\sqrt{\delta}} \int_0^{q_c} \frac{dq}{\sqrt{\delta}} \frac{\frac{q^2}{\delta}}{\frac{q^4}{\delta^2}+1}. \quad (60)$$

When $q_c/\sqrt{\delta} \to \infty$, the integral in Eq. (60) converges logarithmically to $\frac{\pi}{2\sqrt{2}}$ and we obtain

$$\Re \iiint d^3q \frac{1}{q^2(q^2+i\delta)} \to \frac{\sqrt{2}\pi^2}{\sqrt{\delta}}. \quad (61)$$

Therefore, Eq. (60) numerically diverges as $\frac{1}{\sqrt{\delta}}$ for small δ. An example of this kind of divergence is given in the middle right of Figure 9 in the supplementary material[32] for the VBM of β-AlN (IR-active) using the adiabatic equation.

VI. RESULTS ON DIFFERENT SEMICONDUCTORS

We will now examine five different semiconductors: two of which are IR-inactive materials (diamond and silicon) and three of which are IR-active materials (α-AlN, β-AlN, and BN). Results are fully converged and parameter free (for instance, $i\delta \to 0$ is used throughout). Also, in the case of IR-active materials, only the non-adiabatic AHC theory is used since, as outlined previously, the adiabatic theory breaks down in this case.

We have used the local density approximation (LDA) exchange-correlation functional, which is as good as generalized gradient approximation (GGA) functionals (or even better) for the computation of dynamical properties, as shown by He and coworkers.[33] The implementation of the formalism is done in ABINIT (v7.11),[34] using a plane wave basis set and norm-conserving pseudopotentials. For the computation of phonon responses, we have used DFPT.[35,36]

Thermal expansion effects, that can be computed from first principles using DFPT, see, e.g., Ref. 37, contribute only little to the ZPR and temperature-dependence of the electronic structure, as shown, e.g., in Figs. 4.5, 4.9, 4.12, and 4.13 of Ref. 38.

A. IR-inactive materials

1. Diamond

Diamond is a metastable allotrope of carbon where the C atoms are arranged into two interpenetrating face-centered cubic lattices shifted along the body diagonal by $\frac{1}{4}^{\text{th}}$ of its length. The space group associated with this spatial arrangement is $Fd\bar{3}m$ (cubic, 227).

The pseudopotential was generated using the `fhi98PP` code[57] with a 1.5 atomic unit cut-off radius for pseudization. The valence electrons of carbon that were treated explicitly in our *ab initio* calculations are the $2s^2 2p^2 3d^0$ orbitals.

Careful convergence studies (error below 0.5 m hartree per atom on the total energy) led to the use of a $6\times6\times6$ $\mathbf{\Gamma}$-centered Monkhorst-Pack $\mathbf{k}$-point sampling[58] of the BZ and an energy cutoff of 30 hartree for the plane wave basis set. The Perdew and Zunger parametrization of LDA[59] was used. The relaxed lattice parameter is calculated to be 6.652 bohrs, 1.3% below the experimental value of 6.740 bohrs, measured at room temperature[54] (see Table IV for more information on the structural properties).

The electronic band structure was computed at the DFT level and gave a direct bandgap at $\mathbf{\Gamma}$ of 5.67 eV and an indirect $\mathbf{\Gamma} - 0.727\mathbf{X}$ bandgap of 4.25 eV, intrinsically below the experimental bandgap of 5.48 eV at 0 K[60] (see Table V). The phonon

TABLE IV. Convergence parameters for the different compounds studied. The space groups are given in Hermann-Mauguin notation with the number in bracket being the crystallographic index number in international tables. The $\mathbf{k}$-points sampling are homogeneous and $\mathbf{\Gamma}$-centered. All the pseudopotentials in this work use the LDA exchange-correlation functional.

				Lattice parameters (bohrs)			
	Space group	Ecut (hartree)	$\mathbf{k}$-grid	This work (LDA)	Other DFT (LDA)	Other DFT (GGA)	Experiment (300 K)
α-AlN	$P6_3mc$ [186]	35	$6\times6\times6$	5.783/9.255	5.820/9.335[39]	5.913/9.481[40]	5.881/9.415[41]
							5.880/9.409[42]
							5.877/9.411[43]
β-AlN	$F\bar{4}3m$ [216]	35	$6\times6\times6$	8.130	8.205[39]	8.317[40]	8.258[44]
					8.164[45]	8.303[46]	8.277[42]
c-BN	$F\bar{4}3m$ [216]	35	$8\times8\times8$	6.746	6.754[47]	6.852[40]	6.833[48]
					6.752[49]	6.831[50]	
					6.814[51]		
					6.833[52]		
C-d	$Fd\bar{3}m$ [227]	30	$6\times6\times6$	6.652	6.652[8]	6.756[53]	6.740[54]
Si	$Fd\bar{3}m$ [227]	20	$6\times6\times6$	10.170	10.223[55]	10.335[40]	10.26[56]

TABLE V. The direct and indirect (when relevant) DFT electronic bandgaps are compared with other references (theoretical or experimental). The star (*) sign denotes low temperature experiment (below 10 K) and no star means room temperature.

	Direct gap (eV)				Indirect gap (eV)			
	This work	Other DFT			This work	Other DFT		
	LDA	LDA	GGA	Expt.	LDA	LDA	GGA	Expt.
α-AlN	4.691	4.2[61]	4.056[40]	6.28*[62]				
		4.3[63]		6.28*[64]				
		4.41[39]		6.3[44]				
		4.52[65]						
		4.74[46]						
β-AlN	4.677	4.2[66]	3.995[40]		3.308		3.306[40]	
		4.2[63]				3.2[63]		
		4.35[39]				3.2[61]		
		4.75[46]						
c-BN	8.890	8.6[67]		14.5[50]	4.446	4.4[49]	4.450[40]	6.4[68]
		8.7[52]				5.18[52]		6.4[69]
		8.8[49]						
C-d	5.670		5.571[40]	7.3*[60]	4.250		4.113*[40]	5.48*[60]
							4.12*[53]	
Si	2.567	2.52[70]	2.557*[40]	3.378*[71]	0.463	0.45[70]	0.612*[40]	1.17*[71]

frequencies are slightly overestimated (≤4%) with respect to experiment (see Table VI).

For the calculations of the ZPR, we used 10 bands to describe the active space in Eqs. (15) and (17).

The convergence studies with respect to **q**-point integration for the band edges and the direct bandgap of diamond are shown in Figure 6(a), where the densest grid used is a 125 × 125 × 125 **q**-grid (43 680 **q**-points in the irreducible Brillouin-Zone (IBZ)). The Γ^c_{15} state is not the bottom of the conduction band, and therefore, there are other states in the BZ with close energy. This leads to numerical instabilities as the denominator of adiabatic Eq. (15) can diverge for small $i\delta$. To circumvent the issue, we first extrapolated the ZPR to $\delta = 0$ using linear fits and then converged this extrapolated value with respect to **q**-point density. This convergence can be found in Figure 6(b) and shows that large **q**-point grid is required to enter the expected linear regime (see Section V B for more information). The extrapolated ZPR is found to be −277.61 meV.

The VBM (Γ^v_{25}) ZPR converges linearly with **q**-point density and can thus be extrapolated to infinitely dense **q**-grid for each value of $i\delta$ considered. Then, it can be smoothly extrapolated to $\delta = 0$ using a square-root fit, which yields 160.96 meV. The adiabatic direct bandgap ZPR of diamond is thus found to be −438.6 meV.

For the non-adiabatic direct bandgap of diamond, the convergence can be found in Figure 7 and shows that the Γ^c_{15} state converges in a similar way than in the adiabatic case, while the VBM has a flat convergence with respect to **q**-point density and a Lorentzian behavior when $\delta \to 0$. The fitted Lorentzian has three parameters: a multiplicative constant A, the full width at half maximum (FWHM) Γ, and an additive constant B,

$$A\frac{\frac{\Gamma}{2\pi}}{(\frac{\Gamma}{2})^2 + x^2} + B, \tag{62}$$

where here $A = 10.11$, $\Gamma = 0.55$, and $B = 121.90$. The extrapolated ZPRs are −283.23 meV and 133.57 meV for the Γ^c_{15} and Γ^v_{25} states, respectively. This leads to a −415.8 meV renormalization of the direct bandgap due to electron-phonon interaction at 0 K.

TABLE VI. Phonon frequencies at different high symmetry points. All the DFT calculations (this work and references) use the LDA exchange-correlation functional.

		Phonon frequency (cm^{-1})		
	Points	This work	Other DFT	Experiment
α-AlN	$\Gamma_{A_1(TO)}$	609	619[82]	614[83]
	$\Gamma_{E_1(TO)}$	678	677[82]	673[83]
	$\Gamma_{A_1(LO)}$	893	893[82]	893[83]
	$\Gamma_{E_1(LO)}$	924	918[82]	916[83]
β-AlN	Γ_{TO}	661	662[82]	
	Γ_{LO}	907	907[82]	
c-BN	Γ_{TO}	1068	1040[82]	1056[84]
	Γ_{LO}	1299	1285[82]	1304[84]
C-d	Γ_{LTO}	1330	1324[85]	1331,[86] 1332[87]
	X_{TA}	796	800[85]	803,[86] 807[87]
	X_{TO}	1098	1094[85]	1077,[86] 1072[87]
	X_{LAO}	1224	1228[85]	1194,[86] 1184[87]
	L_{TA}	555	561[85]	552[86,88]
	L_{LA}	1076	1080[85]	1035[86,88]
	L_{TO}	1235	1231[85]	1210[86,88]
	L_{LO}	1274	1275[85]	1242[86,88]
Si	Γ_{LTO}	515	517[89]	517[88]
	X_{TA}	136	146[89]	150[88]
	X_{LA}	409	414[89]	410[88]
	X_{TO}	460	466[89]	463[88]
	X_{LO}	409	414[89]	410[88]
	L_{TA}	105	111[89]	114[88]
	L_{LA}	376	378[89]	378[88]
	L_{TO}	490	494[89]	487[88]
	L_{LO}	411	419[89]	417[88]

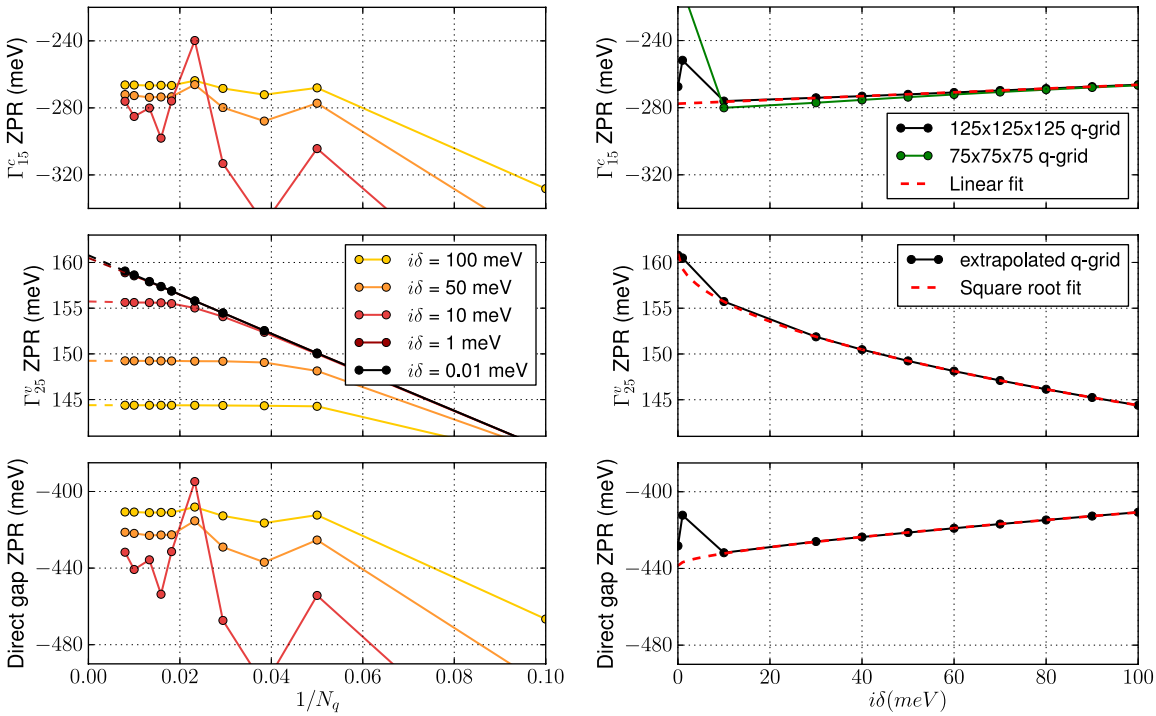

(a) Adiabatic ZPR of direct-gap diamond. (b) $i\delta$ extrapolation of the ZPR.

FIG. 6. Convergence study for the (a) **q**-point grid density and (b) $i\delta$ parameter for the adiabatic direct bandgap ZPR of diamond. The bottom figures are the difference of the two figures above them. The adiabatic ZPR of the direct bandgap of diamond is −438.6 meV.

The convergences of the CBM for diamond are given in Figures 1 and 2 of the supplementary material[32] using the adiabatic and non-adiabatic equations, respectively. For the adiabatic case, the fact that the **q**-convergence is not smooth for relatively small $i\delta$ is attributed to the finite $\mathbf{k}+\mathbf{q}$ sampling. Indeed, when the renormalization is computed at one of the 6 symmetry equivalent CBM **k**-points, the $\mathbf{k}+\mathbf{q}$ sampling is such that the other five equivalent **k**-points are not exactly on the grid. The extrapolated ZPR of the CBM state is −219.24 meV using a square root δ-fit for the adiabatic equa-

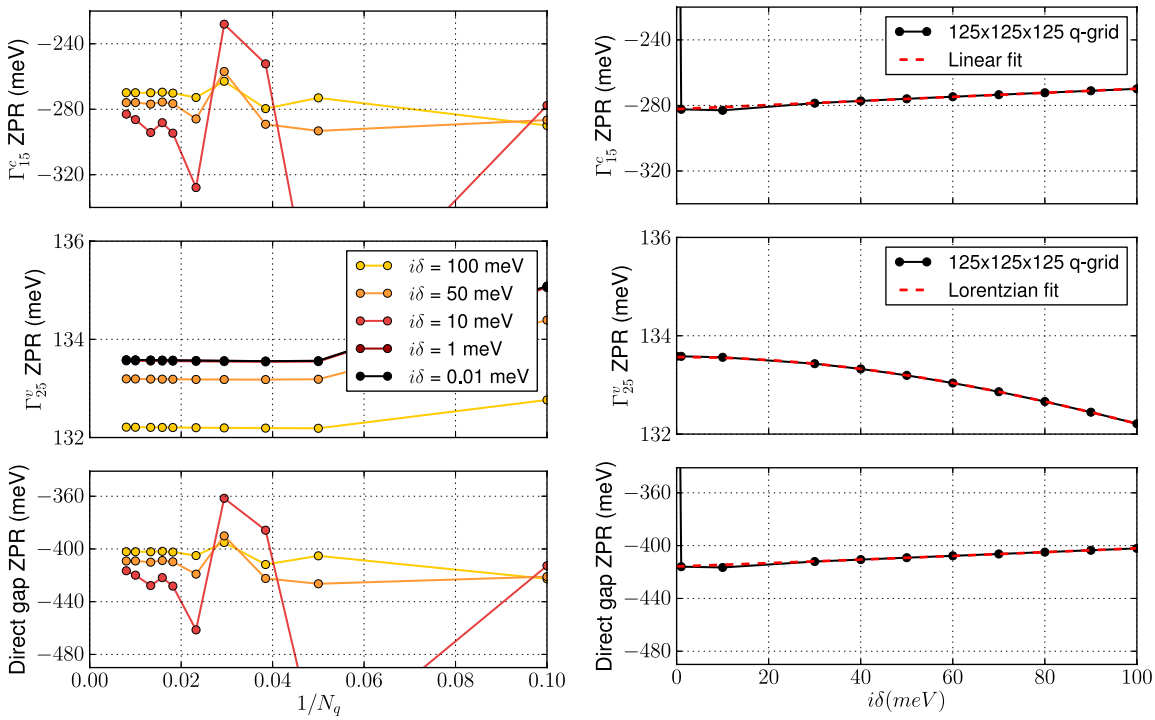

(a) Non-adiabatic ZPR of direct-gap diamond. (b) $i\delta$ extrapolation of the ZPR.

FIG. 7. Convergence study for the (a) **q**-point grid density and (b) $i\delta$ parameter for the non-adiabatic direct bandgap ZPR of diamond. The bottom figures are the difference of the two figures above them. The non-adiabatic ZPR of the direct bandgap of diamond is −415.8 meV.

TABLE VII. ZPR and adiabatic broadening for the different compounds studied at 0 K. The two experimental results for the direct bandgap renormalization of diamond from Ref. 73 are extracted using first or second-derivative line-shape analysis. The two experimental ZPRs for the indirect bandgap of silicon from Ref. 60 are obtained using a mass derivative of the gap and from linear extrapolation to 0 K.

		ZPR (meV)			$(dGap/dT)_{T\to\infty}$ (meV/K)		Broadening (meV)	
Compounds	Gap	Adiabatic	Non-adiabatic	Experimental	Non-adiabatic	Experimental	Adiabatic limit	Experimental
α-AlN	$\mathbf{\Gamma}-\mathbf{\Gamma}$		−377.7	−239[90]	−0.772	−0.83[60,76,90]	117	
β-AlN	$\mathbf{\Gamma}-\mathbf{\Gamma}$		−413.6		−0.763		118	
	$\mathbf{\Gamma}-\mathbf{X}$		−334.4		−0.521		108	
c-BN	$\mathbf{\Gamma}-\mathbf{\Gamma}$		−502.0		−0.639		315	
	$\mathbf{\Gamma}-\mathbf{X}$		−405.6		−0.521		136	
C	$\mathbf{\Gamma}-\mathbf{\Gamma}$	−438.6	−415.8	−320,[73] −450[73]	−0.504	−0.60,[73] −0.69[73]	180	
	$\mathbf{\Gamma}-0.727\mathbf{X}$	−379.3	−329.8	−364,[60] −410[74]	−0.435	−0.54[60]	63	
Si	$\mathbf{\Gamma}-\mathbf{\Gamma}$	−47.1	−42.1		−0.147		31	
	$\mathbf{\Gamma}-0.848\mathbf{X}$	−64.3	−56.2	−53,[92] −62,[60] −64[60]	−0.255	−0.32[79,80]	22	∼35[81]

tion and −196.22 meV using a Lorentzian δ-fit for the non-adiabatic equation (see Table VII for more information). The indirect bandgap ZPR of diamond is thus found to be −380.20 meV and −329.79 meV in the adiabatic and the non-adiabatic approximations, respectively.

The temperature dependence of the direct and indirect bandgaps is reported in Figure 8 for a $75\times75\times75$ **q**-grid and shows that the slope at high temperature for the non-adiabatic renormalization with a Lorentzian extrapolation to $\delta = 0$ is −0.504 meV/K for the direct bandgap and −0.435 meV/K for the indirect one. The phonon-induced broadening $\frac{1}{2\tau_{n\mathbf{k}}^{(adiabatic,RIA)}}$ of Eq. (19) is calculated (with a $75\times75\times75$ **q**-grid) to be 180 meV and 63 meV for the direct and indirect bandgaps of diamond at 0 K, respectively.

Our non-adiabatic result of −329.79 meV for the indirect bandgap ZPR of diamond underestimates the experimental one (−364 meV[60]) by 9.4%. Since our calculation neglects several effects like anharmonicity, non-rigid-ion terms, or many-body *GW* corrections, we are surprisingly close to the experimental value. Actually, depending on the extrapolation scheme, the same experimental data can give widely varying ZPR, ranging from −290 to −510 meV for the indirect bandgap of diamond.[74] The most accurate extrapolation scheme based on 4th-order phonon dispersion yields an experimental ZPR of −410 meV.[74] Our non-adiabatic result at the DFT level would underestimate the experimental one by 20% in that case, closer to what is expected from this level of theory.

The measured slope at high temperature for the indirect bandgap of diamond is −0.54 meV/K.[60] The measured slope at high temperature for the direct bandgap is −0.60 or −0.69 meV/K,[73] depending on the analysis.[75] Our theoretical values for the indirect and direct bandgaps underestimate the experimental ones by 19% and 16%, respectively. We hypothesize that this underestimation of the slope at high temperature for the direct bandgap of diamond is due to the underestimation of the ZPR within DFT. Indeed, as discussed in Ref. 9, the correction brought by *GW* to the ZPR is quite substantial for the direct bandgap (−209 meV). Since the ZPR is directly linked with the slope at high temperature, it is not surprising that we witness such an underestimation with respect to the experimental results. We did not compute such GW correction for ZPR of the indirect bandgap of diamond but expect from the results of Figure 8 to have a smaller correction.

It is worthwhile to note that the complete lack of experimental data for low temperature (T < 100 K) and the relatively large error bars (up to ±10 meV) between 200 K and 350 K generate an uncertainty of several meV on the experimental ZPR.[76] This calls for new, reliable, and wide range temperature

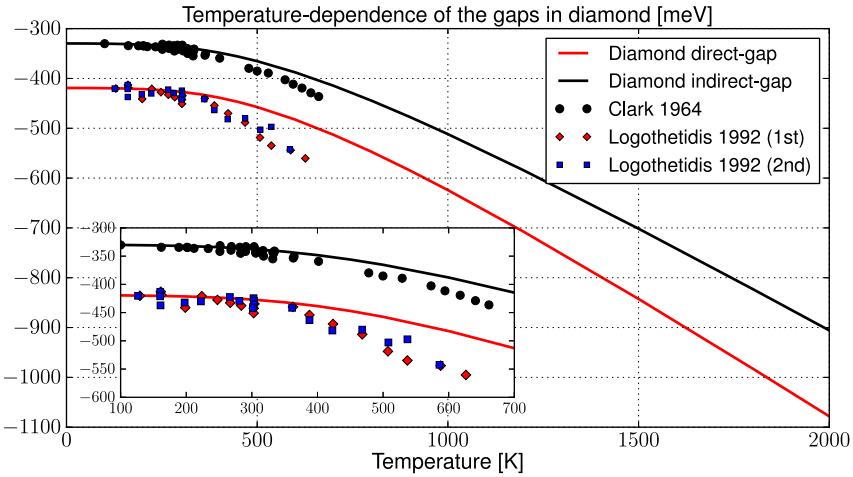

FIG. 8. Temperature dependence of the diamond gaps using the non-adiabatic temperature dependence on a $75\times75\times75$ **q**-grid with Lorentzian extrapolation to vanishing imaginary parameter δ. The slopes at high temperature are −0.504 meV/K for the direct gap of diamond and −0.435 meV/K for the indirect one. The experimental points from the works of Clark *et al.*[72] and Logothetidis *et al.*[73] (using first or second-derivative line-shape analysis) are shifted so that the lowest temperature point matches the theoretical line.

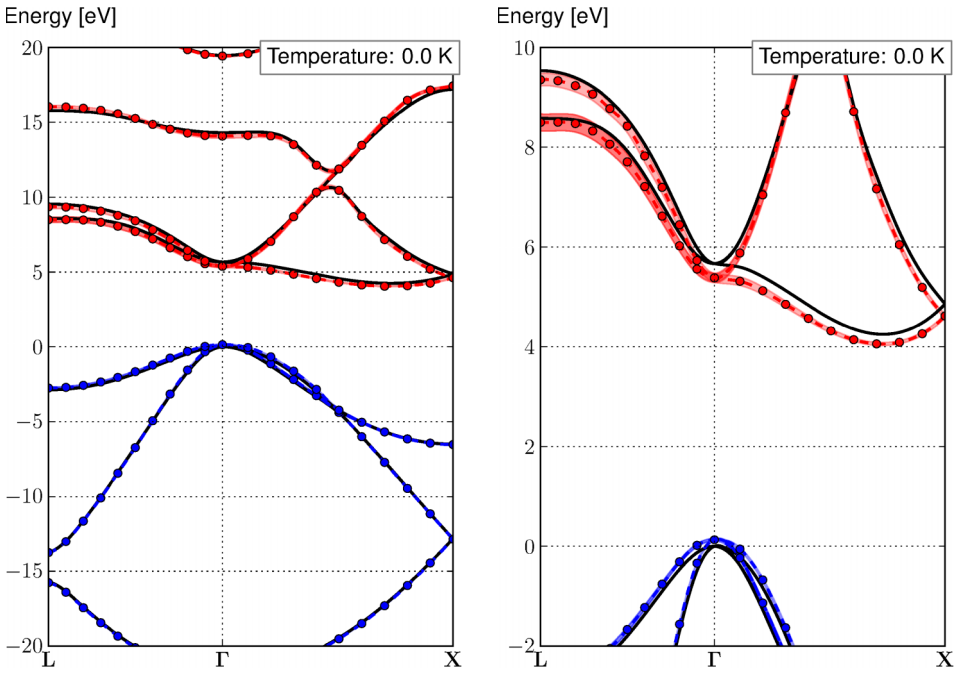

(a) Diamond band structure at 0K.

(b) Zoom of the left-hand side figure.

FIG. 9. Electronic band structure (plain black line), non-adiabatic renormalization (dashed line), and phonon-induced broadening (width around the dashed line) at 0 K using a $75\times75\times75$ **q**-point grid and $\delta\to0$ for diamond, where the dots are the actual renormalization calculation. A spline function is used to connect the renormalization dots.

measurement of the evolution of the bandgap with temperature in diamond. We hope that our theoretical study will stimulate such experimental interest.

Finally, the non-adiabatically renormalized electronic band structure of diamond at 0 K along the $\mathbf{L}-\mathbf{\Gamma}-\mathbf{X}$ high symmetry line is shown in Figure 9 for a $75\times75\times75$ **q**-point grid and a δ extrapolated to zero either linearly (for non-extremal eigenvalues) or with a Lorentzian (for the VBM and CBM).

2. Silicon

Silicon is a tetravalent metalloid widely used in integrated circuits and semiconductor electronics. It has a diamond cubic crystal structure with a $Fd\bar{3}m$ (cubic, 227) space group.

The pseudopotential used for silicon was generated using the `fhi98PP` code[57] with a 1.0247 a.u. cut-off radius for pseudization. The pseudopotential is a Troullier-Martins with the Perdew/Wang[77] parametrization of LDA. The valence electrons of silicon, treated explicitly in the *ab initio* calculations, are the $3s^2 3p^2$ orbitals.

Careful convergence checks (error below 0.5 m hartree per atom on the total energy) lead to the use of a $6\times6\times6$ $\mathbf{\Gamma}$-centered Monkhorst-Pack **k**-point sampling[58] of the BZ and an energy cutoff of 20 hartree for the plane wave basis set. The relaxed lattice parameter is calculated to be 10.170 bohrs, 0.9% below the experimental value, measured at room temperature[56] (see Table IV for more information on the structural properties).

The electronic band structure was computed at the DFT level and gave a direct gap at $\mathbf{\Gamma}$ of 2.567 eV and an indirect $\mathbf{\Gamma}-0.848\mathbf{X}$ gap of 0.463 eV, below the experimental values of 3.378 and 1.17 eV at ~10 K[71] for the direct and indirect gaps, respectively (see Table V). Many *ab initio* simulations have been performed on silicon and give similar values to ours. For example, Ref. 70 got a direct bandgap of 2.52 eV and an indirect one of 0.45 eV, also using the ABINIT software. The phonon frequencies are slightly underestimated with respect to experiment apart for the 136 cm^{-1} X_{TA} mode that underestimates quite strongly the 150 cm^{-1} one (see Table VI).

For the calculations of the ZPR, we used 10 bands to describe the active space in Eqs. (15) and (17). The convergence of the direct bandgaps of silicon is shown in Figure 3 of the supplementary material[32] for the adiabatic equation and gives a linearly δ-extrapolated ZPR of −6.23 meV for the Γ^c_{15} state and a square-root δ-extrapolated ZPR of 40.87 meV for the VBM, thus leading to an adiabatic ZPR of −47.1 meV for the direct bandgap. The non-adiabatic ZPR (see Figure 4 of the supplementary material[32]) is calculated to be −7.36 meV for the Γ^c_{15} state and 34.87 meV for the VBM. The non-adiabatic bandgap ZPR is therefore slightly smaller than the adiabatic one with a value of −42.1 meV. The densest grid used is a $100\times100\times100$ **q**-grid (22 776 **q**-points in the IBZ). The convergences of the adiabatic and non-adiabatic indirect bandgap of silicon are shown in Figures 5 and 6 of the supplementary material,[32] respectively. The adiabatic ZPRs are −23.28 meV for the CBM and 40.87 meV for the VBM, leading to −64.3 meV renormalization of the gap. The non-adiabatic ZPRs are −21.43 meV for the CBM and 34.75 meV for the VBM, leading to a smaller −56.2 meV renormalization of the gap.

Such values can be compared with those of Ref. 55: −57 and −22 meV for the indirect and direct bandgap renormalizations of silicon. These results were obtained using a $4\times4\times4$ supercell within the adiabatic AHC framework. Their results match well those we obtained with the same framework and **q**-grid: −52 and −29 meV for the indirect and direct bandgaps,

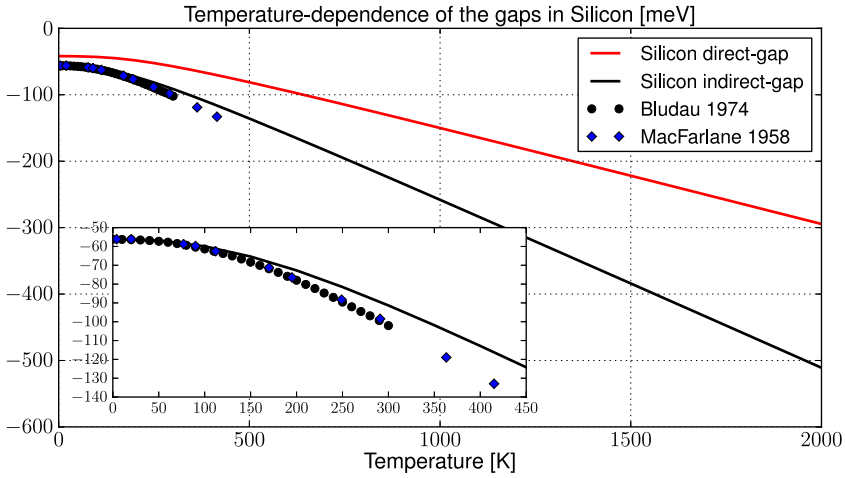

FIG. 10. Adiabatic temperature dependence of the silicon gaps using a 75 ×75×75 **q**-grid and a Lorentzian δ-extrapolation. The slopes at high temperature are −0.147 meV/K for the direct gap of silicon and −0.255 meV/K for the indirect one. The experimental data from Ref. 79 (black circles) and Ref. 80 (blue diamond) are shifted so that the lowest temperature point matches the theoretical line.

respectively (as can also be seen in Figures 3 and 5 of the supplementary material[32]). Earlier, Monserrat and Needs[78] had obtained a ZPR of the indirect bandgap of silicon of −60 meV using a $5 \times 5 \times 5$ supercell, again in fairly good agreement with our results.

The non-adiabatic temperature dependence of direct and indirect $\mathbf{\Gamma} - 0.848\mathbf{X}$ bandgaps obtained with a $75 \times 75 \times 75$ **q**-grid and a Lorentzian δ-extrapolation is reported in Figure 10 and gives slopes at high temperature of −0.147 and −0.255 meV/K, respectively.

The experimental ZPRs of the silicon indirect gap are −62 meV (obtained from mass derivative of the gap) and −64 meV (obtained from linear extrapolation to 0 K[60]). The measured linear slope at high temperature is −0.32 meV/K.[79,80] Those experimental results are larger than the theoretical ones we obtained using the non-adiabatic AHC equation, as expected for DFT calculations. This is related to the underestimation of the ZPR by DFT with respect to GW calculations.

Additionally, we present in Figure 11 the phonon-induced broadening of the direct and indirect gaps of silicon with temperature. The direct and indirect gap broadenings at 0 K are computed to be 31 meV and 23 meV, respectively. The experimental broadening, measured with spectroscopic ellipsometry in Ref. 81 (red dots), is attributed to the broadening of the $E_1 = \mathbf{\Lambda}_3^v - \mathbf{\Lambda}_1^c$ direct transition with temperature. In Ref. 81, it is also mentioned that the measured values at higher temperature (black dots) are difficult to attribute to the broadening of one particular transition since the E_1 gap is nearly degenerate with the $E_0' = \mathbf{\Gamma}_{25'}^v - \mathbf{\Gamma}_{15}^c$ transition. Also, since the ellipsometry measurement is a spectroscopic measurement, it can only probe direct transitions. In consequence, we should compare the broadening results (both black and red dots) with the silicon red line (direct-gap E_0').

Finally, the non-adiabatically renormalized electronic band structure of silicon at 0 K along the $\mathbf{L} - \mathbf{\Gamma} - \mathbf{X}$ high symmetry line is shown in Figure 12 for a $75 \times 75 \times 75$ **q**-point grid and δ extrapolated to zero.

B. IR-active materials

1. *Aluminum nitride*

Aluminum nitride in the wurtzite structure (α-AlN) has one of the widest gaps among nitride semiconductors. It has a $P6_3mc$ (hexagonal, 186) space group. The zincblende form of aluminum nitride (β-AlN) has an $F\bar{4}3$ m (cubic, 216) space group and has been reported to be experimentally metastable.[42] We will study the temperature-dependence properties of these two phases using the non-adiabatic framework.

The aluminum and nitrogen pseudopotentials were generated using the `fhi98PP` code[57] with a 1.0247 a.u. cut-off radius for pseudization and a maximum angular channel of

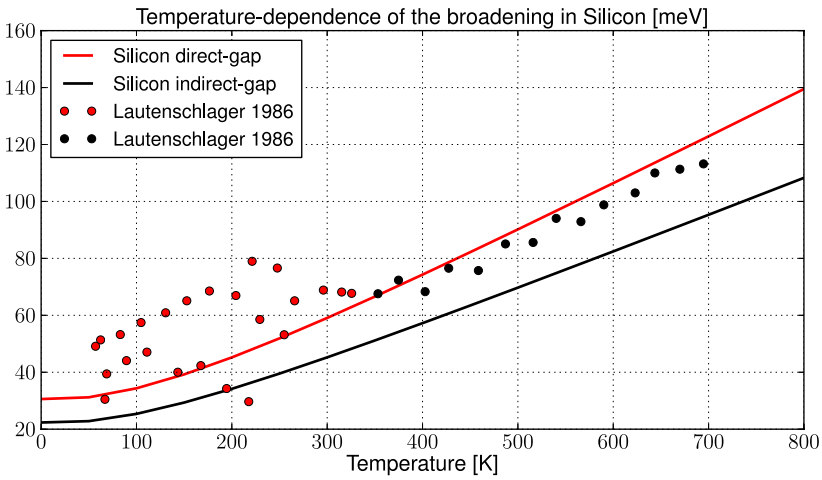

FIG. 11. Temperature dependence of the silicon gaps adiabatic broadening using a 75×75×75 **q**-grid. The experimental data (red and black dots) are from Ref. 81.

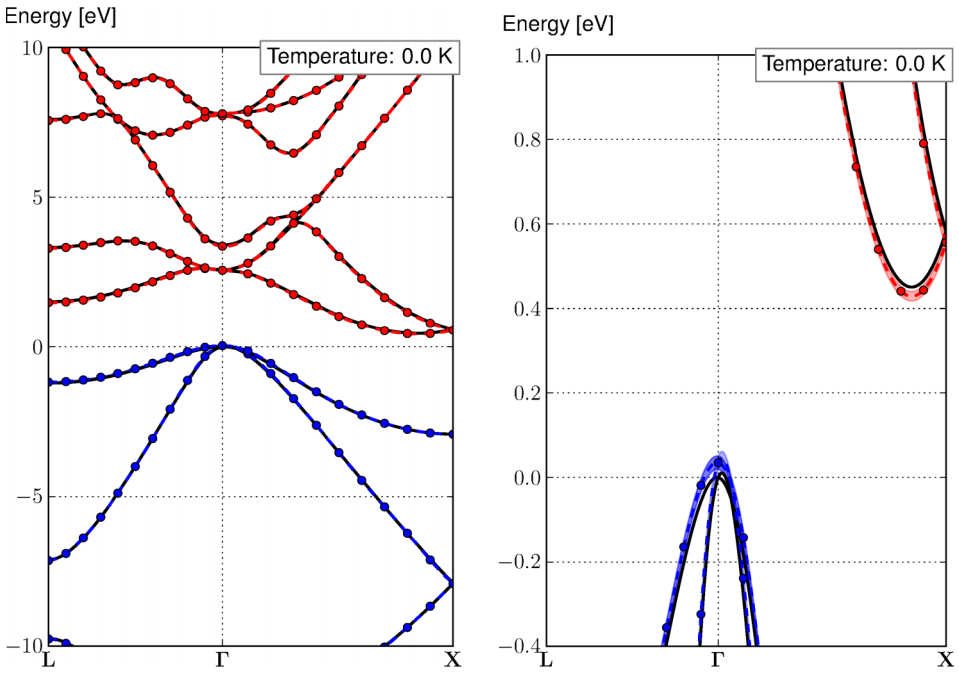

(a) Silicon band structure at 0K.

(b) Zoom of the left-hand side figure.

FIG. 12. Electronic band structure (plain black line), non-adiabatic renormalization (dashed line), and phonon-induced broadening (width around the dashed line) at 0 K with a $75\times75\times75$ **q**-point grid and $\delta\to0$ for silicon, where the dots are the actual renormalization calculation. A spline function is used to connect the renormalization dots.

$l = 2$. Both are Troullier-Martins pseudopotentials that use the Perdew/Wang[77] parametrization of the LDA. The valence electrons of aluminum and nitrogen treated explicitly in the calculations are the $3s^23p^1$ and $2s^22p^3$ orbitals, respectively.

Convergence checks (error below 0.5 m hartree per atom on the total energy) lead to the use of a $6\times6\times6$ **Γ**-centered Monkhorst-Pack **k**-point sampling[58] of the BZ and an energy cutoff of 35 hartree for the plane wave basis set. We used 18 bands to describe the active space in Eqs. (15) and (17).

The relaxed lattice parameters are found to be a = 5.783 and c = 9.255 bohrs for α-AlN and a = 8.130 bohrs for β-AlN. These values are at maximum 2.3% below the experimental ones (see Table IV).

For α-AlN, we find a direct gap at **Γ** of 4.691 eV. This is well above the 4.056 eV gap computed within the Materials Project using GGA[40] but well in the range of other LDA gaps (see Table V). These DFT values naturally underestimate the experimental gap of 6.28 eV at 5 K.[62,64] We obtain for the zincblende β-AlN an indirect $\mathbf{\Gamma}-\mathbf{X}$ bandgap of 3.308 eV, almost identical to the Materials Project value (see Table V). The value we obtained for the direct gap at **Γ** of 4.677 eV is a bit above most LDA values reported in the table. However, one must consider that the 4.2 eV LDA direct gap calculation performed in Ref. 63 is done at the experimental lattice parameter, in contrast to ours. Our phonon frequencies are within 1% of the experimental ones for α-AlN (see Table VI). Note that no experimental values were found for the metastable zincblende β-AlN. Still, our results agree very well with those of another DFT study, as presented in Table VI.

The **q**-point convergence for the adiabatic ZPR of the direct gap of α-AlN is shown in Figure 7 of the supplementary material.[32] It diverges at dense **q**-grid, as expected since AlN is an IR-active material. The non-adiabatic direct bandgap ZPR shown in Figure 8 of the supplementary material[32] converges linearly with the **q**-point density and has a Lorentzian behavior for $\delta\to0$. We thus find a non-adiabatic ZPR of −183.5 meV for the CBM and of 194.2 meV for the VBM, leading to a ZPR of the direct bandgap of α-AlN of −377.7 meV. The densest **q**-grid used is a $34\times34\times34$ grid (2052 **q**-points in the IBZ).

For the same reason than α-AlN, the β-AlN adiabatic ZPR diverges, as shown in Figures 9 and 11 of the supplementary material.[32] The non-adiabatic direct bandgap ZPR shown in Figure 10 of the supplementary material[32] converges linearly with the **q**-point density and the $\delta\to0$ behavior can be fitted by a line or a Lorentzian, as appropriate for the state studied. We obtain a ZPR of −187.54 meV for the CBM and of 226.08 meV for the VBM, thus leading to a direct bandgap ZPR of −413.62 meV for β-AlN. The non-adiabatic indirect bandgap ZPR of β-AlN is shown in Figure 12 of the supplementary material[32] and converges linearly with the **q**-point density and has a Lorentzian behavior for $\delta\to0$. The extrapolation gives a ZPR of −108.36 meV for the CBM, resulting in a −334.4 meV ZPR of the indirect bandgap of β-AlN (see Table VII for more information). The densest **q**-grid used is a $100\times100\times1000$ grid (22 776 **q**-points in the IBZ).

The temperature dependence of the three gaps is reported in Figures 13 and 14. Their slopes at high temperature are found to be −0.772, −0.521, and −0.763 meV/K for the direct gap of α-AlN, the indirect bandgap of β-AlN, and the direct bandgap of β-AlN, respectively.

The phonon-induced broadening is found to be 117 meV for the direct bandgap of α-AlN using a $34\times34\times34$ **q**-grid. The broadening of the direct and indirect bandgaps of β-AlN at 0 K is 118 meV and 108 meV, respectively, for a $75\times75\times75$ **q**-grid.

The experimental ZPR for α-AlN has been obtained by linearly extrapolating to 0 K the change of the direct bandgap with temperature and yields a value of −239 meV, with a

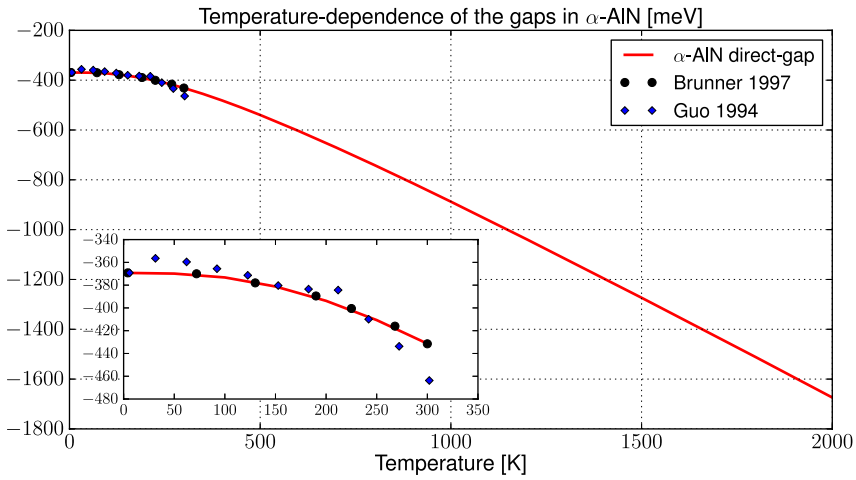

FIG. 13. Non-adiabatic temperature dependence of the α-AlN gaps using a $34\times34\times34$ **q**-grid and a Lorentzian extrapolation to $\delta = 0$. The slope at high temperature is −0.772 meV/K for the direct gap of α-AlN. The experimental data from Ref. 90 (black circles) and Ref. 91 (blue diamond) are shifted so that the lowest temperature point matches the theoretical line.

slope at high temperature of −0.83 meV/K,[60,76,90] in relatively good agreement with our −0.772 meV/K value. The obvious disagreement with our theoretical value for the direct bandgap ZPR (−369 meV versus −239 meV) can be attributed to the fact that the experimental data set measured by Brunner *et al.*[90] is very scarce and within a narrow temperature range (4-298 K). As pointed out by Pässler[76] for this compounds: *"this illustrates the great importance of extending experimental measurements in wide bandgap materials far beyond room temperature."*

Finally, we show in Figures 15 and 16 the non-adiabatically renormalized electronic band structure at 0 K along the highest symmetry path $\mathbf{\Gamma} - \mathbf{M}$ for α-AlN and along the $\mathbf{L} - \mathbf{\Gamma} - \mathbf{X}$ path of β-AlN. The thickness of the lines is associated with the lifetime of the electronic state computed with Eq. (19).

2. Boron nitride

BN exists in various crystalline forms. Its most stable phase, under normal conditions, is a hexagonal layered structure. The cubic boron nitride (c-BN) has a zincblende structure and is isoelectronic to diamond. We will only study the c-BN polymorph here.

The boron and nitrogen pseudopotentials were generated using the `fhi98PP` code[57] with a 1.0247 a.u. cut-off radius for pseudization and a maximum angular channel of $l = 2$. Both of them are Troullier-Martins pseudopotentials that use the Perdew/Wang[77] parametrization of LDA. The valence electrons of boron and nitrogen treated explicitly in the calculations are the $2s^2 2p^1$ and $2s^2 2p^3$ orbitals, respectively.

Careful convergence checks (error below 0.5 m hartree per atom on the total energy) lead to the use of an $8\times8\times8$ $\mathbf{\Gamma}$-centered Monkhorst-Pack **k**-point sampling[58] of the BZ and an energy cutoff of 35 hartree for the plane wave basis set.

The relaxed lattice parameter is found to be 6.746 bohrs, 1.3% below the experimental value of 6.833 bohrs[48] (see Table IV for more information on the structural properties).

The electronic band structure was computed at the DFT level and yields a direct gap at $\mathbf{\Gamma}$ of 8.890 eV and an indirect $\mathbf{\Gamma} - \mathbf{X}$ gap of 4.446 eV, below the experimental value of 6.4 eV for the indirect gap at 300 K[69] (see Table V). The phonon frequencies are within 2% of the experimental ones for c-BN (see Table VI). In the ZPR calculations, we use 18 bands to describe the active space (see Eqs. (15) and (17)).

The c-BN is also an IR-active material and therefore its adiabatic ZPR diverge, as shown in Figures 16 and 14 of the supplementary material.[32] The non-adiabatic direct bandgap ZPR shown in Figure 13 of the supplementary material[32] converges linearly with the **q**-point density and the $\delta \to 0$ behavior can be fitted by a line or a Lorentzian, as appropriate for the state studied. This yields a ZPR of −301.48 meV for

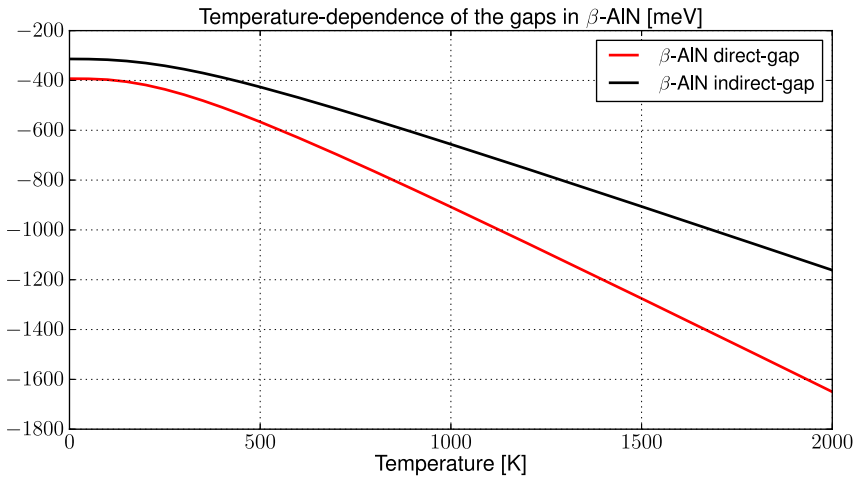

FIG. 14. Non-adiabatic temperature dependence of the β-AlN gaps using a $75\times75\times75$ **q**-grid and a Lorentzian extrapolation to $\delta = 0$. The slopes at high temperature are −0.763 meV/K for the direct gap of β-AlN and −0.521 meV/K for the indirect one. No experimental data were found in the literature.

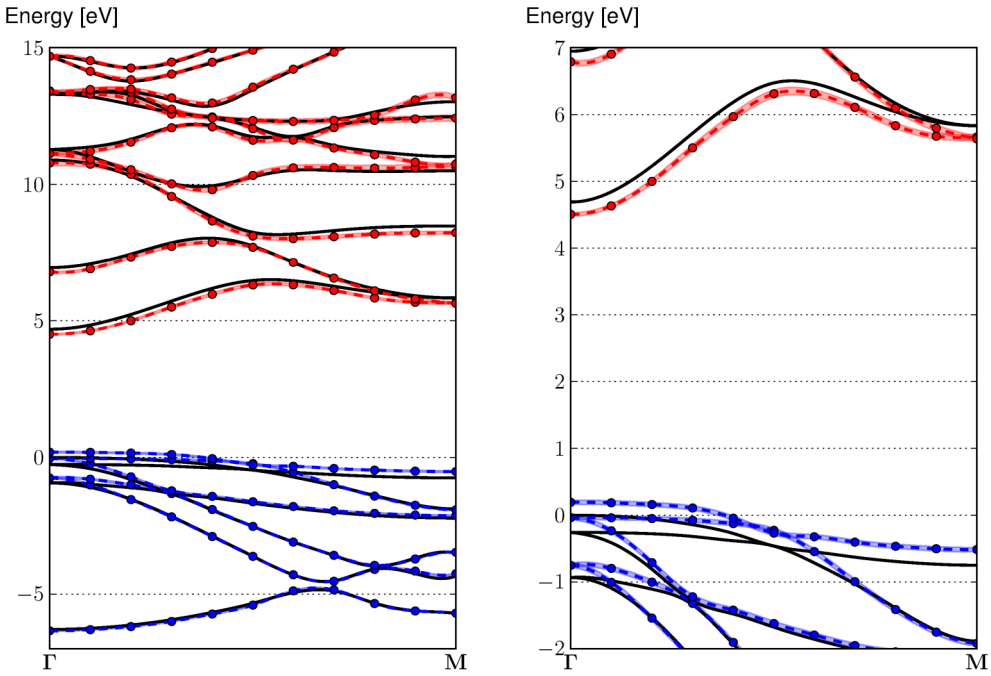

(a) α-AlN band structure at 0K.

(b) Zoom of the left-hand side figure.

FIG. 15. Electronic band structure (plain black line), non-adiabatic renormalization (dashed line), and phonon-induced broadening (width around the dashed line) at 0 K with a $34\times34\times34$ **q**-point grid and $\delta \to 0$ for α-AlN, where the dots are the actual renormalization calculation. A spline function is used to connect the renormalization dots.

the Γ_1^c state and of 200.5 meV for the VBM, thus leading to a direct bandgap ZPR of −502.0 meV for c-BN. The non-adiabatic indirect bandgap ZPR of c-BN is shown in Figure 15 of the supplementary material[32] and converges linearly with the **q**-point density and has a Lorentzian behavior for $\delta \to 0$. This yields a ZPR of −205.08 meV for the CBM, thus leading to an indirect bandgap ZPR of −405.6 meV for c-BN (see Table VII for more information). The densest **q**-grid used is a $100 \times 100 \times 1000$ grid (22 776 **q**-points in the IBZ).

The non-adiabatic temperature dependence of direct and indirect gaps is reported in Figure 17 for a $75 \times 75 \times 75$ **q**-grid

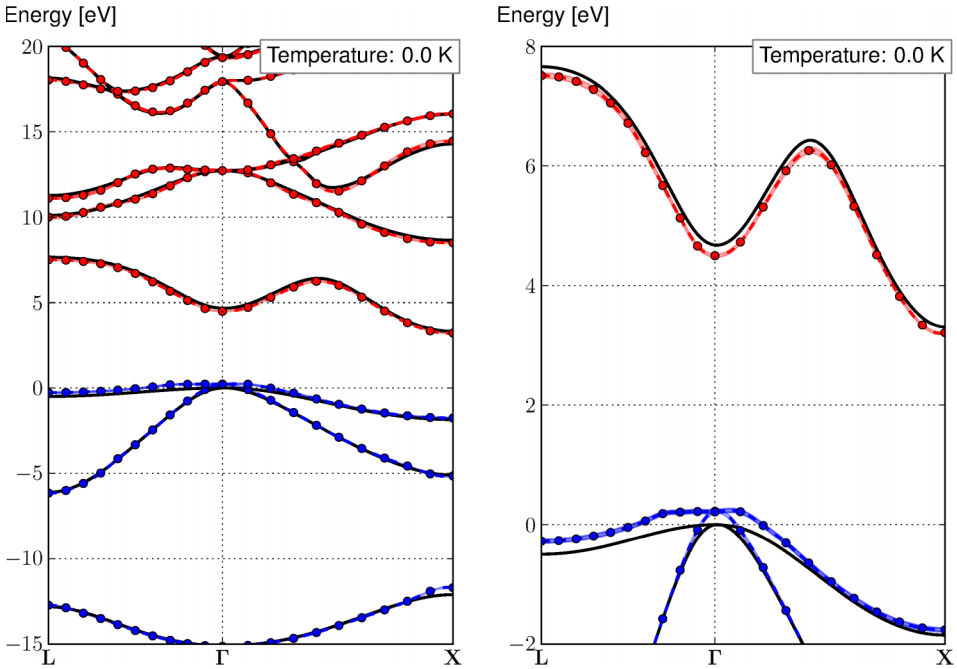

(a) β-AlN band structure at 0K.

(b) Zoom of the left-hand side figure.

FIG. 16. Electronic band structure (plain black line), non-adiabatic renormalization (dashed line), and phonon-induced broadening (width around the dashed line) at 0 K using a $75\times75\times75$ **q**-point grid and $\delta \to 0$ for β-AlN, where the dots are the actual renormalization calculation. A spline function is used to connect the renormalization dots.

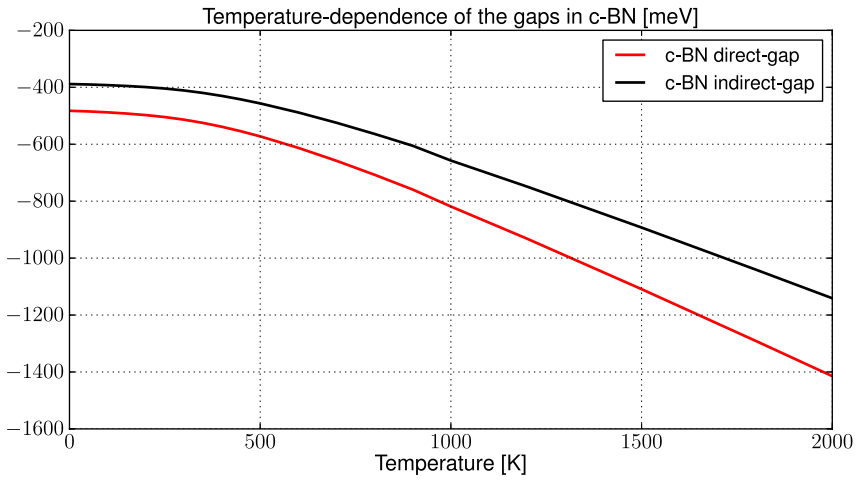

FIG. 17. Non-adiabatic temperature dependence of the c-BN gaps using a $75\times75\times75$ **q**-grid and a Lorentzian extrapolation to $\delta = 0$. The slopes at high temperature are −0.639 meV/K for the direct gap of c-BN and −0.521 meV/K for the indirect one. No experimental data were found in the literature.

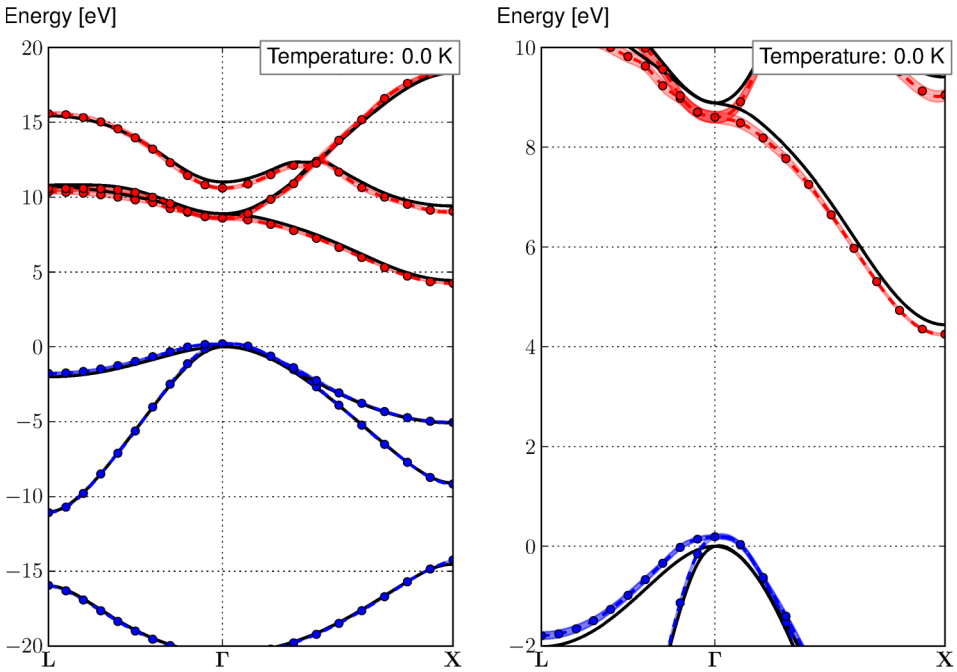

(a) c-BN band structure at 0K. (b) Zoom of the left-hand side figure.

FIG. 18. Electronic band structure (plain black line), non-adiabatic renormalization (dashed line), and phonon-induced broadening (width around the dashed line) at 0 K using a $75\times75\times75$ **q**-point grid and $\delta \to 0$ for β-AlN, where the dots are the actual renormalization calculation. A spline function is used to connect the renormalization dots.

with extrapolation to $\delta = 0$ and gives slopes at high temperature of −0.639 and −0.521 meV/K, respectively. The phonon-induced broadening is calculated to be 315 meV and 136 meV for the direct and indirect bandgaps of c-BN at 0 K, respectively, using a $75 \times 75 \times 75$ **q**-grid.

Finally, the non-adiabatic renormalized electronic band structure of c-BN at 0 K along the **L** − **Γ** − **X** high-symmetry line is shown in Figure 18 for a $75 \times 75 \times 75$ **q**-point grid and $\delta \to 0$.

VII. CONCLUSIONS

In the present work, we demonstrated that electron-phonon renormalization of eigenenergies within the adiabatic AHC framework diverges in IR-inactive materials due to the presence of a residual Born effective charge in *ab initio* calculations stemming from the finite **k**-point sampling of the BZ. After proposing a solution to this issue, we analyze theoretically the adiabatic and non-adiabatic convergences with **q**-point sampling and numerical broadening parameter $i\delta$, depending on the IR activity of the materials, taking into account whether the state renormalized is at band extrema or elsewhere. We demonstrate that unlike the adiabatic AHC formalism, the non-adiabatic AHC formalism has no divergence problem for IR-active materials and should therefore be used in these cases.

We believe that such breakdown of the adiabatic theory is not an artifact of the perturbative expansion of DFPT but should also be observed in the FP and MD cases. Indeed, in such cases, the electric field associated with any IR-active (LO) phonon mode present in IR-active materials will induce a spatially extended linear potential change. For sufficiently large supercells, pathological phenomena will appear. In particular, it is well established that such linear potential change has to be

dealt carefully, with issues related to cross convergence of the strength of the electric field and sampling of wave vectors (or size of supercell).[93–95]

We then use our analysis of the convergence behavior of the renormalization to devise a systematic procedure to converge the ZPR and apply it to five semiconductors/insulators (diamond, silicon, and the α and β phases of aluminum nitride and boron nitride). For these materials, we present the non-adiabatic renormalized electronic band structure (at the density functional theory level) due to electron-phonon coupling (see Eqs. (16) and (17)) as well as the phonon induced lifetime in the adiabatic limit (see Eq. (19)). We also obtain the temperature dependence of the direct and indirect bandgaps of these materials and compare them with experiment when available.

We find that the non-adiabatic ZPR at the DFT level systematically underestimates the experimental results (by less than 10%), except in α-AlN, where the theoretical value is larger than the experimental value of Ref. 90. The latter observation raises doubts about the accuracy of the experimental result in that case, where the experimental ZPR was obtained by linear extrapolation to 0 K of gaps within a very limited temperature range (4-298 K, where the linear regime was not yet achieved). We hope that our work will motivate experimental studies relying on wider temperature ranges for the estimation of the ZPR. We also think that the present approach might be useful in the future to compute more evolved temperature-dependent properties, such as optical properties.

ACKNOWLEDGMENTS

We acknowledge stimulating discussions with the participants of the *2015 CECAM workshop on Electron-vibration coupling: theoretical and numerical challenges*, especially F. Giustino and M. Côté. This work was supported by the FRS-FNRS through a FRIA fellowship (S.P.) and a FNRS fellowship (Y.G.) as well as the FRQNT through a postdoctoral research fellowship (J.L.J.). Moreover, A.M. would like to acknowledge the financial support from the Futuro in Ricerca Grant No. RBFR12SW0J of the Italian Ministry of Education, University, and Research. The authors would like to thank Yann Pouillon and Jean-Michel Beuken for their valuable technical support and help with the test and build systems of ABINIT. Computational resources have been provided by the supercomputing facilities of the Université catholique de Louvain (CISM/UCL) and the Consortium des Équipements de Calcul Intensif en Fédération Wallonie Bruxelles (CECI) funded by the Fonds de la Recherche Scientifique de Belgique (FRS-FNRS) under Grant No. 2.5020.11.

APPENDIX A: DERIVATION OF THE RENORMALIZATION FACTOR

1. Minimization of the variational second-order electronic energy

The variational second-order electronic energy without non-linear core correction can be written as (see Eq. (60) of Ref. 31)

$$E^{(2)}_{-\mathbf{q},\mathbf{q}} = \frac{\Omega_0}{(2\pi)^3}\int_{BZ} d\mathbf{k} \sum_n^{occ} s_n \Big(\langle u^{(1)}_{n\mathbf{k},\mathbf{q}} | H^{(0)}_{\mathbf{k}+\mathbf{q},\mathbf{k}+\mathbf{q}} - \varepsilon^{(0)}_{n\mathbf{k}} | u^{(1)}_{n\mathbf{k},\mathbf{q}} \rangle + \langle u^{(1)}_{n\mathbf{k},\mathbf{q}} | v^{(1)}_{ext,\mathbf{k}+\mathbf{q},\mathbf{k}} | u^{(0)}_{n\mathbf{k}} \rangle + \langle u^{(0)}_{n\mathbf{k}} | v^{(1)}_{ext,\mathbf{k},\mathbf{k}+\mathbf{q}} | u^{(1)}_{n\mathbf{k},\mathbf{q}} \rangle$$
$$+ \langle u^{(0)}_{n\mathbf{k}} | v^{(2)}_{ext,\mathbf{k},\mathbf{k}} | u^{(0)}_{n\mathbf{k}} \rangle \Big) + \frac{1}{2}\int_{\Omega_0} \frac{d^2(n\varepsilon_{xc})}{dn^2}\Big|_{n^{(0)}(\mathbf{r})} |n^{(1)}_{\mathbf{q}}(\mathbf{r})|^2 d\mathbf{r} + 2\pi\Omega_0 \sum_{\mathbf{G}\neq 0} \frac{|n^{(1)}_{\mathbf{q}}(\mathbf{G})|^2}{|\mathbf{q}+\mathbf{G}|^2} + n^{(1)*}_{\mathbf{q}}(\mathbf{G}=0)\frac{2\pi}{q} w^{(1)}_{\mathbf{q}}$$
$$+ n^{(1)}_{\mathbf{q}}(\mathbf{G}=0)\frac{2\pi}{q} w^{(1)*}_{\mathbf{q}} + 2\pi\Omega_0 \frac{|n^{(1)}_{\mathbf{q}}(\mathbf{G}=0)|^2}{q^2}, \tag{A1}$$

where we follow the notation of Ref. 31, i.e., the superscripts (0) and (1) refer to the unperturbed and first-order perturbation (here the nucleus motion) of the periodic part of the wavefunction, s_n is the spin degeneracy factor, $v^{(1)}_{ext,\mathbf{k}+\mathbf{q},\mathbf{k}}$ is the first-order perturbed potential external to the electronic system that includes the ionic potential

$$v^{(1)}_{ext,\mathbf{k}+\mathbf{q},\mathbf{k}} = v^{(1)}_{sep,\mathbf{k}+\mathbf{q},\mathbf{k}} + \bar{v}^{(1)}_{loc,\mathbf{q}}, \tag{A2}$$

and ε_{xc} is the exchange-correlation energy per electron

$$\frac{d^2(n\varepsilon_{xc})}{dn^2}\Big|_{n^{(0)}} = \frac{dv_{xc}}{dn}\Big|_{n^{(0)}}. \tag{A3}$$

The second-order change of the nonlocal potential $v^{(2)}_{sep,\mathbf{k},\mathbf{k}}$ is given in Eq. (54) of Ref. 31.

The first-order change of the local potential of Eq. (24) for $\mathbf{G} = 0$ can be written as

$$\lim_{q\to 0} \bar{v}^{(1)}_{loc,\mathbf{q}}(0) = \frac{4\pi}{\Omega_0}\frac{1}{q} w^{(1)}_{\mathbf{q}}, \tag{A4}$$

with

$$w^{(1)}_{\mathbf{q}} = -i\frac{q_\alpha}{q} e^{-i\mathbf{q}\cdot\boldsymbol{\tau}_\kappa}\Big(- Z_\kappa + \frac{q^2}{4\pi} C_\kappa + O(q^4)\Big). \tag{A5}$$

To write Eq. (A1) in a more compact form, we define the following vectors:

$$\mathbf{x}_i \triangleq \langle \mathbf{G} | u^{(1)}_{n\mathbf{k},\mathbf{q}} \rangle, \tag{A6}$$

$$\mathbf{u}_i \triangleq s_n w_{n\mathbf{k}} \langle \mathbf{G} | u^{(0)}_{n\mathbf{k}} \rangle, \tag{A7}$$

$$\mathbf{w}_i \triangleq s_n w_{n\mathbf{k}} \langle \mathbf{G}|v^{(1)}_{ext,\mathbf{k}+\mathbf{q},\mathbf{k}}|u^{(0)}_{n\mathbf{k}}\rangle, \tag{A8}$$

where $w_{n\mathbf{k}}$ is the weight of the $\mathbf{k}$-point (which is zero for unoccupied states) and where the index i stands for the combined plane wave component $\mathbf{G}$, band index n, and wave-vector $\mathbf{k}$ indices. It will later be useful to note that

$$\mathbf{u}^\dagger\mathbf{x} = \frac{\Omega_0}{(2\pi)^3}\int_{BZ} d\mathbf{k} \sum_n^{occ} s\langle u^{(0)}_{n\mathbf{k}}|u^{(1)}_{n\mathbf{k},\mathbf{q}}\rangle = \frac{\Omega_0}{2} n^{(1)}_{\mathbf{q}}(\mathbf{G}=0). \tag{A9}$$

In addition, we define the following scalars:

$$a \triangleq \frac{8\pi}{\Omega_0}\frac{1}{q^2}, \tag{A10}$$

$$b \triangleq \frac{4\pi}{\Omega_0 q} w^{(1)}_{\mathbf{q}}, \tag{A11}$$

$$c \triangleq \frac{\Omega_0}{(2\pi)^3}\int_{BZ} d\mathbf{k} \sum_n^{occ} s_n \langle u^{(0)}_{n\mathbf{k}}|v^{(2)}_{ext,\mathbf{k},\mathbf{k}}|u^{(0)}_{n\mathbf{k}}\rangle. \tag{A12}$$

Finally, we define a matrix $\mathbf{A}$ such that

$$\begin{aligned}\mathbf{x}^\dagger\mathbf{A}\mathbf{x} \triangleq \frac{\Omega_0}{(2\pi)^3}\int_{BZ} d\mathbf{k} \sum_n^{occ} s_n \langle u^{(1)}_{n\mathbf{k},\mathbf{q}}|H^{(0)}_{\mathbf{k}+\mathbf{q},\mathbf{k}+\mathbf{q}} \\ - \varepsilon^{(0)}_{n\mathbf{k}}|u^{(1)}_{n\mathbf{k},\mathbf{q}}\rangle + \frac{1}{2}\int_{\Omega_0} \frac{d^2(n\varepsilon_{xc})}{dn^2}\Big|_{n^{(0)}(\mathbf{r})} |n^{(1)}_{\mathbf{q}}(\mathbf{r})|^2 d\mathbf{r} \\ + 2\pi\Omega_0 \sum_{\mathbf{G}\neq 0} \frac{|n^{(1)}_{\mathbf{q}}(\mathbf{G})|^2}{|\mathbf{q}+\mathbf{G}|^2}.\end{aligned} \tag{A13}$$

Using the above definitions (Eqs. (A6)-(A8) and (A10)-(A13)), Eq. (A1) can be re-expressed in short-hand notation

$$\begin{aligned}E^{(2)}_{-\mathbf{q},\mathbf{q}} = \mathbf{x}^\dagger\mathbf{A}\mathbf{x} + a(\mathbf{u}^\dagger\mathbf{x})(\mathbf{x}^\dagger\mathbf{u}) \\ + (b\mathbf{x}^\dagger\mathbf{u} + \mathbf{x}^\dagger\mathbf{w} + (c.c.)) + c.\end{aligned} \tag{A14}$$

The physical value of the first-order perturbed periodic part of the wavefunction $\mathbf{x}$ is the one that minimizes $E^{(2)}_{-\mathbf{q},\mathbf{q}}$ (we will refer to it as $\mathbf{x}_1$),

$$\begin{aligned}\delta E^{(2)}_{-\mathbf{q},\mathbf{q}} &= (\{\delta\mathbf{x}_1^\dagger(\mathbf{A}\mathbf{x}_1 + (b + a(\mathbf{u}^\dagger\mathbf{x}_1))\mathbf{u} + \mathbf{w})\} + (c.c.)) \\ &= 0.\end{aligned} \tag{A15}$$

The real part of the quantity between curly brackets is therefore zero

$$\Re\{\delta\mathbf{x}_1^\dagger(\mathbf{A}\mathbf{x}_1 + (b + a(\mathbf{u}^\dagger\mathbf{x}_1))\mathbf{u} + \mathbf{w})\} = 0. \tag{A16}$$

For the preceding relation to hold for any $\delta\mathbf{x}$, the quantity in parenthesis () must be zero,

$$\mathbf{A}\mathbf{x}_1 + (b + a(\mathbf{u}^\dagger\mathbf{x}_1))\mathbf{u} + \mathbf{w} = 0, \tag{A17}$$

which leads to

$$\mathbf{x}_1 = -(b + a(\mathbf{u}^\dagger\mathbf{x}_1))\mathbf{A}^{-1}\mathbf{u} - \mathbf{A}^{-1}\mathbf{w}. \tag{A18}$$

We define

$$\mathbf{x}_1 \triangleq \mathbf{x}_{1a} + \mathbf{x}_{1b}, \tag{A19}$$

where

$$\mathbf{x}_{1a} \triangleq -\mathbf{A}^{-1}\mathbf{w}, \tag{A20}$$

and we are left with

$$\mathbf{x}_{1b} = -(b + a(\mathbf{u}^\dagger(\mathbf{x}_{1a} + \mathbf{x}_{1b})))\mathbf{A}^{-1}\mathbf{u}. \tag{A21}$$

By defining

$$b' = b + a(\mathbf{u}^\dagger\mathbf{x}_{1a}), \tag{A22}$$

Eq. (A21) becomes

$$\mathbf{x}_{1b} = -(b' + a(\mathbf{u}^\dagger\mathbf{x}_{1b}))\mathbf{A}^{-1}\mathbf{u}. \tag{A23}$$

By multiplying the preceding equation by $\mathbf{u}^\dagger$ and isolating $\mathbf{u}^\dagger\mathbf{x}_{1b}$, we obtain

$$\mathbf{u}^\dagger\mathbf{x}_{1b} = \frac{-b'\mathbf{u}^\dagger\mathbf{A}^{-1}\mathbf{u}}{1 + a(\mathbf{u}^\dagger\mathbf{A}^{-1}\mathbf{u})}. \tag{A24}$$

Substituting this result back in Eq. (A23), we obtain $\mathbf{x}_{1b}$,

$$\mathbf{x}_{1b} = \frac{-b'}{1 + a(\mathbf{u}^\dagger\mathbf{A}^{-1}\mathbf{u})}\mathbf{A}^{-1}\mathbf{u} \tag{A25}$$

and, using Eqs. (A19), (A20), and (A22), we finally have

$$\mathbf{x}_1 = -\mathbf{A}^{-1}\mathbf{w} + \frac{-b + a(\mathbf{u}^\dagger\mathbf{A}^{-1}\mathbf{w})}{1 + a(\mathbf{u}^\dagger\mathbf{A}^{-1}\mathbf{u})}\mathbf{A}^{-1}\mathbf{u}. \tag{A26}$$

Substituting Eq. (A17) into Eq. (A14), we obtain the value of $E^{(2)}_{-\mathbf{q},\mathbf{q}}$ at the minimum $\mathbf{x}_1$,

$$\tilde{E}^{(2)}_{-\mathbf{q},\mathbf{q}} \triangleq b^*\mathbf{u}^\dagger\mathbf{x}_1 + \mathbf{w}^\dagger\mathbf{x}_1 + c. \tag{A27}$$

Then, substituting Eq. (A26) into Eq. (A27), we finally obtain

$$\begin{aligned}\tilde{E}^{(2)}_{-\mathbf{q},\mathbf{q}} = -\mathbf{w}^\dagger\mathbf{A}^{-1}\mathbf{w} + c + \frac{(-b\mathbf{w}^\dagger\mathbf{A}^{-1}\mathbf{u} + (c.c.))}{1 + a\mathbf{u}^\dagger\mathbf{A}^{-1}\mathbf{u}} \\ + \frac{-|b|^2\mathbf{u}^\dagger\mathbf{A}^{-1}\mathbf{u} + a|\mathbf{w}^\dagger\mathbf{A}^{-1}\mathbf{u}|^2}{1 + a\mathbf{u}^\dagger\mathbf{A}^{-1}\mathbf{u}}.\end{aligned} \tag{A28}$$

2. Macroscopic dielectric constant

From Eq. (B3) of Ref. 31 and Eq. (A9), we can deduce that the second-derivative of the total energy with respect to a monochromatic electric field of wavevector $\mathbf{q}$ located inside the first BZ is

$$\begin{aligned}E^{ef(2)}_{-\mathbf{q},\mathbf{q}} = \frac{\Omega_0}{(2\pi)^3}\int_{BZ} d\mathbf{k} \sum_n^{occ} s_n\Big(\langle u^{(1)}_{n\mathbf{k},\mathbf{q}}|H^{(0)}_{\mathbf{k}+\mathbf{q},\mathbf{k}+\mathbf{q}} - \varepsilon^{(0)}_{n\mathbf{k}}|u^{(1)}_{n\mathbf{k},\mathbf{q}}\rangle + \langle u^{(1)}_{n\mathbf{k},\mathbf{q}}|u^{(0)}_{n\mathbf{k}}\rangle + \langle u^{(0)}_{n\mathbf{k}}|u^{(1)}_{n\mathbf{k},\mathbf{q}}\rangle\Big) + 2\pi\Omega_0\frac{|n^{(1)}_{\mathbf{q}}(\mathbf{G}=0)|^2}{\mathbf{q}^2} \\ + \frac{1}{2}\int_{\Omega_0} \frac{d^2(n\varepsilon_{xc})}{dn^2}\Big|_{n^{(0)}(\mathbf{r})} |n^{(1)}_{\mathbf{q}}(\mathbf{r})|^2 d\mathbf{r} + 2\pi\Omega_0 \sum_{\mathbf{G}\neq 0} \frac{|n^{(1)}_{\mathbf{q}}(\mathbf{G})|^2}{|\mathbf{q}+\mathbf{G}|^2} = \mathbf{x}^\dagger\mathbf{A}\mathbf{x} + \mathbf{x}^\dagger\mathbf{u} + \mathbf{u}^\dagger\mathbf{x} + a(\mathbf{u}^\dagger\mathbf{x})(\mathbf{x}^\dagger\mathbf{u}),\end{aligned} \tag{A29}$$

where we have used the short-hand notation defined before. In the same spirit as Eq. (A15), we can find the value of $\mathbf{x}$ that minimizes Eq. (A29) (that we will call $\mathbf{x}_2$) and deduce

$$\mathbf{A}\mathbf{x}_2 + a(\mathbf{u}^\dagger\mathbf{x}_2)\mathbf{u} + \mathbf{u} = 0, \tag{A30}$$

which gives

$$\mathbf{x}_2 = (-a(\mathbf{u}^\dagger\mathbf{x}_2) - 1)\mathbf{A}^{-1}\mathbf{u}. \tag{A31}$$

Multiplying Eq. (A30) by $\mathbf{u}^\dagger$ and isolating $\mathbf{x}_2$ allows us to obtain

$$\mathbf{x}_2 = -\frac{\mathbf{A}^{-1}\mathbf{u}}{1 + a(\mathbf{u}^\dagger\mathbf{A}^{-1}\mathbf{u})}. \tag{A32}$$

Substituting Eq. (A30) and then Eq. (A32) into Eq. (A29), we obtain the value of $E^{ef(2)}_{-\mathbf{q},\mathbf{q}}$ at the minimum $\mathbf{x}_2$,

$$\tilde{E}^{ef(2)}_{-\mathbf{q},\mathbf{q}} \triangleq \mathbf{u}^\dagger\mathbf{x}_2 = -\frac{\mathbf{u}^\dagger\mathbf{A}^{-1}\mathbf{u}}{1 + a(\mathbf{u}^\dagger\mathbf{A}^{-1}\mathbf{u})}. \tag{A33}$$

We can also define a total energy where the divergent $\mathbf{G} = 0$ hartree contribution has been removed. The resulting term is analytic

$$E^{ef,an(2)}_{-\mathbf{q},\mathbf{q}} = \mathbf{x}^\dagger\mathbf{A}\mathbf{x} + \mathbf{x}^\dagger\mathbf{u} + \mathbf{u}^\dagger\mathbf{x} \tag{A34}$$

$$= \mathbf{u}^\dagger\mathbf{x} + \mathbf{x}^\dagger(\mathbf{A}\mathbf{x} + \mathbf{u}). \tag{A35}$$

The location $\mathbf{x}_3$ of the minimum of $E^{ef,an(2)}_{-\mathbf{q},\mathbf{q}}$ can be obtained in a similar way to Eq. (A32),

$$\mathbf{A}\mathbf{x}_3 + \mathbf{u} = 0 \Rightarrow \mathbf{x}_3 = \mathbf{A}^{-1}\mathbf{u}. \tag{A36}$$

Substituting Eq. (A36) into Eq. (A34), we obtain the value of $E^{ef,an(2)}_{-\mathbf{q},\mathbf{q}}$ at the minimum $\mathbf{x}_3$,

$$\tilde{E}^{ef,an(2)}_{-\mathbf{q},\mathbf{q}} = -\mathbf{u}^\dagger\mathbf{A}^{-1}\mathbf{u}. \tag{A37}$$

Comparing Eqs. (A33) and (A37), we deduce

$$\tilde{E}^{ef(2)}_{-\mathbf{q},\mathbf{q}} = \frac{\tilde{E}^{ef,an(2)}_{-\mathbf{q},\mathbf{q}}}{1 - a\tilde{E}^{ef,an(2)}_{-\mathbf{q},\mathbf{q}}}. \tag{A38}$$

The polarizability $\chi(\mathbf{r},\mathbf{r}')$ is defined as the microscopic response to a change of external potential that gives the total change of electronic density $\delta n(\mathbf{r})$,

$$\delta n(\mathbf{r}) = \int_{\Omega_0} \chi(\mathbf{r},\mathbf{r}')\delta v_{ext}(\mathbf{r}') \tag{A39}$$

$$\Rightarrow \frac{\delta n(\mathbf{r})}{\delta v_{ext}(\mathbf{r}')} = \chi(\mathbf{r},\mathbf{r}'). \tag{A40}$$

Transforming to reciprocal space and taking the $(\mathbf{G},\mathbf{G}') = (\mathbf{0},\mathbf{0})$ matrix element yield

$$n^{(1)}_{\mathbf{q}}(\mathbf{G} = \mathbf{0}) = \chi_{\mathbf{q}}(\mathbf{G} = \mathbf{0},\mathbf{G}' = \mathbf{0}), \tag{A41}$$

where (1) superscript refers to the first-order perturbation in the external potential due to the electric field. Taking a long wavelength monochromatic electric field as the perturbation

$$v^{(1)}_{ext,\mathbf{q}}(\mathbf{r},\mathbf{r}') = e^{i\mathbf{q}\cdot\mathbf{r}}\delta(\mathbf{r},\mathbf{r}') \tag{A42}$$

gives in reciprocal space

$$v^{(1)}_{ext,\mathbf{k}+\mathbf{q},\mathbf{k}}(\mathbf{G},\mathbf{G}') = \delta_{\mathbf{G},\mathbf{G}'}. \tag{A43}$$

Also, Eq. (A33) tells us that

$$\tilde{E}^{ef(2)}_{-\mathbf{q},\mathbf{q}} = \mathbf{u}^\dagger\mathbf{x}_2 \tag{A44}$$

$$= \frac{\Omega_0}{2} n^{(1)}_{\mathbf{q}}(\mathbf{0}) \tag{A45}$$

$$= \frac{\Omega_0}{2} \chi_{\mathbf{q}}(\mathbf{0},\mathbf{0}), \tag{A46}$$

where the second and third equalities stem from Eq. (A9) and (A41), respectively.

The dielectric function is defined as (see Eq. (23) of Ref. 96, for example)

$$\varepsilon^{-1}_{\mathbf{q}}(\mathbf{G},\mathbf{G}') = \delta_{\mathbf{G},\mathbf{G}'} + \frac{4\pi}{|\mathbf{q}+\mathbf{G}|^2}\chi_{\mathbf{q}}(\mathbf{G},\mathbf{G}'), \tag{A47}$$

and the macroscopic dielectric function, which is an average response to an applied field is (see Eq. (15) of Ref. 96, for example)

$$\varepsilon_M(\mathbf{q}) = \frac{1}{\varepsilon^{-1}_{\mathbf{q}}(\mathbf{0},\mathbf{0})}. \tag{A48}$$

Therefore, using Eqs. (A10), (A46), and (A47), we obtain

$$\varepsilon_M(\mathbf{q}) = \frac{1}{1 + a\tilde{E}^{ef(2)}_{-\mathbf{q},\mathbf{q}}}. \tag{A49}$$

Using Eqs. (A37) and (A38) finally yields

$$\varepsilon_M(\mathbf{q}) = 1 - a\tilde{E}^{ef,an(2)}_{-\mathbf{q},\mathbf{q}} \tag{A50}$$

$$= 1 + a(\mathbf{u}^\dagger\mathbf{A}^{-1}\mathbf{u}). \tag{A51}$$

3. Born effective charge

Following the phenomenological discussion of Born and Huang (see p. 265 of Ref. 23), in the long-wavelength limit, we can expand the total energy density E_{tot} (including the vacuum energy) quadratically with respect to the ionic displacement $U_{\kappa\alpha}$ of each atom κ in each direction α and with respect to the macroscopic electric field $\mathcal{E}_\alpha$ in each direction α,

$$E_{tot} = \frac{1}{2}\sum_{\kappa\kappa'}\sum_{\gamma\delta} U^*_{\kappa\gamma} C^{\text{an}}_{\substack{\kappa\gamma\\ \kappa'\delta}} U_{\kappa'\delta} - \frac{\Omega_0}{8\pi}\sum_{\gamma\delta}\mathcal{E}_\gamma\epsilon_{\gamma\delta}\mathcal{E}_\delta - \sum_{\kappa\gamma,\delta} U^*_{\kappa\gamma} Z^*_{\kappa\gamma,\delta}\mathcal{E}_\delta, \tag{A52}$$

where Ω_0 is the volume, $C^{\text{an}}_{\substack{\kappa\alpha\\ \kappa'\beta}} = \frac{\partial^2 E}{\partial R_{\kappa\alpha} R_{\kappa'\beta}}$ is the analytic interatomic force constant (IFC), $\epsilon_{\alpha\beta} = \frac{\partial^2 E}{\partial\mathcal{E}_\alpha\mathcal{E}_\beta}$ is the dielectric function, and $Z^*_{\kappa\alpha,\beta} = \frac{\partial^2 E}{\partial R_{\kappa\alpha}\mathcal{E}_\beta}$ the Born effective charge. $C^{\text{an}}_{\substack{\kappa\alpha\\ \kappa'\beta}}$ is associated to the second-order energy (see Eq. (A1)) where the non-analytic terms in $\mathbf{q}$ have been removed

$$E^{an(2)}_{-\mathbf{q},\mathbf{q}} = \frac{1}{2}\frac{\partial^2 E^{an}}{\partial R_{\kappa\alpha}\partial R_{\kappa\alpha}} \triangleq \mathbf{x}^\dagger\mathbf{A}\mathbf{x} + \mathbf{x}^\dagger\mathbf{w} + \mathbf{w}^\dagger\mathbf{x} + c. \tag{A53}$$

The solution $\mathbf{x}_4$ that minimizes Eq. (A53) is

$$\mathbf{x}_4 = -\mathbf{A}^{-1}\mathbf{w}, \tag{A54}$$

which leads to the following value for $E^{an(2)}_{-\mathbf{q},\mathbf{q}}$ at the variational minimum:

$$\tilde{E}^{an(2)}_{-\mathbf{q},\mathbf{q}} \triangleq -\mathbf{w}^\dagger\mathbf{A}^{-1}\mathbf{w} + c = C^{\text{an}}_{\kappa\alpha}. \tag{A55}$$

We now define the electric displacement $\mathcal{D} \triangleq \mathcal{E} + 4\pi\mathcal{P}$ and the polarizability

$$\mathcal{P}_\alpha \triangleq -\frac{1}{\Omega_0}\frac{\partial(E + \frac{\Omega_0}{8\pi}\mathcal{E}^2)}{\partial\mathcal{E}_\alpha}, \tag{A56}$$

where we have excluded the energy of the electric field in vacuum. We can combine this with the absence of free charge ($\boldsymbol{\nabla}\cdot\mathcal{D}(\mathbf{r}) = 0 \Rightarrow \mathbf{q}\cdot\mathcal{D}(\mathbf{q}) = 0$) and magnetic field ($\boldsymbol{\nabla}\times\mathcal{E}(\mathbf{r}) = 0 \Rightarrow \mathbf{q}\times\mathcal{E}(\mathbf{q}) = \mathbf{0}$) to deduce the form of the electric field from Eq. (A52),

$$\mathcal{E}_\alpha = -\frac{4\pi}{\Omega_0}\frac{\sum_{\kappa\gamma,\delta}U^*_{\kappa\gamma}Z^*_{\kappa\gamma,\delta}q_\delta}{\sum_{\gamma\delta}q_\gamma\epsilon_{\gamma\delta}q_\delta}q_\alpha. \tag{A57}$$

Substituting Eq. (A57) into Eq. (A52) yields

$$E^{(2)}_{-\mathbf{q},\mathbf{q}} = \tilde{E}^{an(2)}_{-\mathbf{q},\mathbf{q}} + \frac{2\pi}{\Omega_0}\frac{(\sum_\gamma Z^*_{\kappa\alpha,\gamma}q_\gamma)^2}{\sum_{\gamma\delta}q_\gamma\epsilon_{\gamma\delta}q_\delta}. \tag{A58}$$

We also introduce a mixed term

$$\tilde{E}^{mix(2)}_{-\mathbf{q},\mathbf{q}} \triangleq -\mathbf{w}^\dagger\mathbf{A}^{-1}\mathbf{u}. \tag{A59}$$

Injecting Eqs. (A59), (A55), and (A37) into Eq. (A28), we can express $E^{(2)}_{-\mathbf{q},\mathbf{q}}$ at the minimum as

$$\tilde{E}^{(2)}_{-\mathbf{q},\mathbf{q}} = \tilde{E}^{an(2)}_{-\mathbf{q},\mathbf{q}} + \frac{(b\tilde{E}^{mix(2)}_{-\mathbf{q},\mathbf{q}} + (c.c.))}{1 - a\tilde{E}^{ef,an(2)}_{-\mathbf{q},\mathbf{q}}} + \frac{a|\tilde{E}^{mix(2)}_{-\mathbf{q},\mathbf{q}}|^2 + |b|^2\tilde{E}^{ef,an(2)}_{-\mathbf{q},\mathbf{q}}}{1 - a\tilde{E}^{ef,an(2)}_{-\mathbf{q},\mathbf{q}}}, \tag{A60}$$

where the numerator of this equation should be a square to establish the connection with the effective charges $Z^*_{\kappa\alpha,\gamma}$ of Eq. (A58). To obtain this link, we can compare Eqs. (A10) and (A11), which yields

$$|b|^2 = \frac{2\pi}{\Omega_0}a|w^{(1)}_{\mathbf{q}}|^2. \tag{A61}$$

Thus, Eq. (A60) becomes

$$\tilde{E}^{(2)}_{-\mathbf{q},\mathbf{q}} = \tilde{E}^{an(2)}_{-\mathbf{q},\mathbf{q}} - \frac{2\pi}{\Omega_0}|w^{(1)}_{\mathbf{q}}|^2 + \frac{\left(b\tilde{E}^{mix(2)}_{-\mathbf{q},\mathbf{q}} + (c.c.)\right)}{\varepsilon_M(\mathbf{q})} + \frac{a|\tilde{E}^{mix(2)}_{-\mathbf{q},\mathbf{q}}|^2 + \frac{2\pi}{\Omega_0}|w^{(1)}_{\mathbf{q}}|^2}{\varepsilon_M(\mathbf{q})}, \tag{A62}$$

where we have introduced the macroscopic dielectric function using Eqs. (A51) and (A37). The second term will be canceled by a contribution from the Ewald ion-ion energy to the lowest order in $\mathbf{q}$ and can therefore be included in the analytic part[31]

$$\tilde{E}^{Ew,an(2)}_{-\mathbf{q},\mathbf{q}} = \tilde{E}^{an(2)}_{-\mathbf{q},\mathbf{q}} - \frac{2\pi}{\Omega_0}|w^{(1)}_{\mathbf{q}}|^2. \tag{A63}$$

The non-analytic term in $\mathbf{q} = 0$, i.e., the remainder of $\tilde{E}^{(2)}_{-\mathbf{q},\mathbf{q}}$, can be written as

$$\frac{1}{q^2\varepsilon_M(\mathbf{q})}\frac{2\pi}{\Omega_0}|qw^{(1)}_{\mathbf{q}} + 2\tilde{E}^{mix(2)*}_{-\mathbf{q},\mathbf{q}}|^2, \tag{A64}$$

where we have replaced a and b by their definition Eqs. (A10) and (A11).

For vanishing $\mathbf{q}$, we have at the lowest order (see Eq. (A5))

$$w^{(1)}_{\mathbf{q}} = \frac{q_\alpha}{q}iZ_\kappa + O(\mathbf{q}). \tag{A65}$$

Moreover, the macroscopic dielectric constant can be written as

$$\varepsilon_M(\mathbf{q}) = \frac{1}{q^2}\sum_{\gamma\delta}q_\gamma\varepsilon_{\gamma\delta}q_\delta. \tag{A66}$$

Eq. (A62) thus becomes

$$\tilde{E}^{(2)}_{-\mathbf{q},\mathbf{q}} = \tilde{E}^{Ew,an(2)}_{-\mathbf{q},\mathbf{q}} + \frac{2\pi}{\Omega_0}\frac{|q_\alpha Z_\kappa - 2i\tilde{E}^{mix(2)*}_{-\mathbf{q},\mathbf{q}}|^2}{\sum_{\gamma\delta}q_\gamma\varepsilon_{\gamma\delta}q_\delta}, \tag{A67}$$

where we have obtained the form desired, suitable for comparison with Eq. (A58).

By making this comparison, we deduce

$$\sum_\gamma Z^*_{\kappa\alpha,\gamma}q_\gamma = q_\alpha Z_\kappa + 2i\tilde{E}^{mix(2)}_{-\mathbf{q},\mathbf{q}}, \tag{A68}$$

where we took the complex conjugate of the quantity in the norm of Eq. (A67).

The total Born effective charge is the sum of the ionic charge on the atom κ and the electronic charge belonging to this atom

$$\sum_\gamma Z^*_{\kappa\alpha,\gamma}q_\gamma = \sum_\gamma(Z_\kappa\delta_{\alpha\gamma} + \Delta Z_{\kappa\alpha,\gamma})q_\gamma, \tag{A69}$$

which naturally gives

$$2i\tilde{E}^{mix(2)}_{-\mathbf{q},\mathbf{q}} = \sum_\gamma\Delta Z_{\kappa\alpha,\gamma}q_\gamma. \tag{A70}$$

The last equation leads, in short hand notation, to the following relation (see Eq. (A59)):

$$-\mathbf{u}^\dagger\mathbf{A}^{-1}\mathbf{w} = \frac{i}{2}\sum_\gamma\Delta Z_{\kappa\alpha,\gamma}q_\gamma. \tag{A71}$$

Finally, to the lowest order in $\mathbf{q}$, we deduce from the preceding relation, Eqs. (A10) and (A11),

$$b - a\mathbf{u}^\dagger\mathbf{A}^{-1}\mathbf{w} = \sum_\gamma\frac{4\pi iq_\gamma}{\Omega_0q^2}(Z_\kappa + \Delta Z_{\kappa\alpha,\gamma}) \tag{A72}$$

$$= \sum_\gamma\frac{4\pi iq_\gamma}{\Omega_0q^2}Z^*_{\kappa\alpha,\gamma}. \tag{A73}$$

4. Derivation of Eq. (27)

The first-order Hartree potential diverges as $1/q$ because of a residual electric charge in the first-order density. The first-order density at $\mathbf{G} = 0$ can be written using Eq. (A9) as

$$n^{(1)}_{\mathbf{q}}(0) = \frac{2}{\Omega_0}\mathbf{u}^\dagger\mathbf{x}_1, \tag{A74}$$

and Eq. (A26) as

$$n^{(1)}_{\mathbf{q}}(0) = \frac{2}{\Omega_0}\left(-\mathbf{u}^\dagger\mathbf{A}^{-1}\mathbf{w} - \frac{(b - a(\mathbf{u}^\dagger\mathbf{A}^{-1}\mathbf{w}))}{1 + a(\mathbf{u}^\dagger\mathbf{A}^{-1}\mathbf{u})}\mathbf{u}^\dagger\mathbf{A}^{-1}\mathbf{u}\right). \tag{A75}$$

Using Eqs. (A51), (A66), (A71), and (A73), we have

$$n^{(1)}_{\mathbf{q}}(0) = \frac{2}{\Omega_0}\left(\frac{i}{2}\sum_\gamma\Delta Z_{\kappa\alpha,\gamma}q_\gamma - \frac{\sum_\gamma\frac{4\pi i}{\Omega_0q^2}Z^*_{\kappa\alpha,\gamma}q_\gamma}{\frac{1}{q^2}\sum_{\gamma\delta}q_\gamma\epsilon_{\gamma\delta}q_\delta}\mathbf{u}^\dagger\mathbf{A}^{-1}\mathbf{u}\right). \tag{A76}$$

Using Eq. (A51) to replace $\mathbf{u}^\dagger\mathbf{A}^{-1}\mathbf{u}$ by $\frac{\varepsilon_M(\mathbf{q})-1}{a}$ and then Eqs. (A10), (A66), and (A69), we finally deduce

$$n^{(1)}_{\mathbf{q}}(0) = -\sum_\gamma \frac{iq_\gamma}{\Omega_0}\Big(Z_\kappa\delta_{\alpha\gamma} - \frac{Z^*_{\kappa\alpha,\gamma}}{\frac{1}{q^2}\sum_{\gamma\delta}q_\gamma\epsilon_{\gamma\delta}q_\delta}\Big). \quad \text{(A77)}$$

The first-order Hartree term

$$v^{(1)}_{H,\mathbf{q}}(\mathbf{0}) = 4\pi\frac{n^{(1)}_{\mathbf{q}}}{q^2} \quad \text{(A78)}$$

can then be renormalized to account for the slow $\mathbf{k}$-point convergence of the Born effective charges by enforcing effective charge neutrality within the primitive cell. To do so, we introduce the average Born effective charge per atom

$$\bar{Z}_{\alpha\gamma} = \frac{1}{N_{at}}\sum_\kappa Z^*_{\kappa\alpha,\gamma}, \quad \text{(A79)}$$

where N_{at} is the number of atoms in the primitive cell and subtract it from $Z^*_{\kappa\alpha,\gamma}$,

$$v^{ren(1)}_{H,\mathbf{q}}(\mathbf{0}) = -\sum_\gamma \frac{4\pi iq_\gamma}{\Omega_0 q^2}\Big(Z_\kappa\delta_{\alpha\gamma} - \frac{(Z^*_{\kappa\alpha,\gamma}-\bar{Z}_{\alpha\gamma})}{\frac{1}{q^2}\sum_{\gamma\delta}q_\gamma\epsilon_{\gamma\delta}q_\delta}\Big), \quad \text{(A80)}$$

which finally gives

$$v^{ren(1)}_{H,\mathbf{q}}(\mathbf{0}) = v^{(1)}_{H,\mathbf{q}}(\mathbf{0})\frac{\sum_\gamma q_\gamma\Big(Z_\kappa\delta_{\alpha\gamma} - \frac{(Z^*_{\kappa\alpha,\gamma}-\bar{Z}_{\alpha\gamma})}{\frac{1}{q^2}\sum_{\delta,\xi}q_\delta\epsilon_{\delta\xi}q_\xi}\Big)}{\sum_\gamma q_\gamma\Big(Z_\kappa\delta_{\alpha\gamma} - \frac{Z^*_{\kappa\alpha,\gamma}}{\frac{1}{q^2}\sum_{\delta,\xi}q_\delta\epsilon_{\delta\xi}q_\xi}\Big)}. \quad \text{(A81)}$$

APPENDIX B: BEHAVIOR OF THE ZPR WITH THE SHIFTED PARABOLA MODEL

In this appendix, we study the behavior of the shifted parabola energy model presented in Eq. (36) to mimic the ZPR of IR-active or -inactive materials at points of the BZ that are not VBM nor CBM.

In spherical coordinates, Eq. (36) can be re-expressed as

$$\varepsilon(\mathbf{q}) = q^2 - 2qq_0\cos\theta, \quad \text{(B1)}$$

where we have chosen the shift $\mathbf{q}_0$ along the z-Cartesian axis. This function vanishes when $\mathbf{q} = 0$ or $q = 2q_0\cos\theta$. The last root is a sphere centered around $\mathbf{q_0}$ with radius q_0.

1. Integration on the spherical shell of poles

In this section, the convergence behavior of the ZPR of an IR-active material is analyzed in the case $\delta = 0$. The poles of the integrand of the ZPR form a sphere centered around $\mathbf{q} = \mathbf{q_0}$. To study their impact, we introduce the new variable $\tilde{\mathbf{q}} = \mathbf{q} - \mathbf{q_0}$ and express the ZPR as an integral on a sphere of radius q_c,

$$\int_0^{q_c} d\tilde{q}\int_0^\pi d\theta\int_{-\pi}^\pi d\phi\frac{\sin(\theta)}{(\tilde{\mathbf{q}}+\mathbf{q_0})^2}\frac{\tilde{q}^2}{\tilde{q}^2-q_0^2} = 2\pi\int_0^{q_c} d\tilde{q}\frac{\tilde{q}^2}{\tilde{q}^2-q_0^2}\int_0^\pi d\theta\frac{\sin\theta}{\tilde{q}^2+2qq_0\cos\theta+q_0^2}. \quad \text{(B2)}$$

The radial part of Eq. (B2) can be integrated to

$$-\frac{2\pi}{q_0}\int_0^{q_c} d\tilde{q}\frac{\tilde{q}}{\tilde{q}^2-q_0^2}\ln\Big(\frac{|\tilde{q}+q_0|}{|\tilde{q}-q_0|}\Big). \quad \text{(B3)}$$

As we would like to understand the behavior of the poles when integrated, we restrict the integral on a small spherical shell around $\tilde{q} = 0$, with $q_0 - \Delta < \tilde{q} < q_0 + \Delta$. Expressing everything in terms of a new variable $u = \tilde{q} - q_0$, we obtain

$$-2\pi\int_{-\Delta}^{\Delta} du\frac{1}{u}\frac{1+\frac{u}{q_0}}{u+2q_0}\ln\Big(\frac{|2q_0+u|}{|u|}\Big), \quad \text{(B4)}$$

which may be re-written as

$$\int_{-\Delta}^{\Delta} duF(u)\frac{1}{u} + G(u)\frac{\ln(|u|)}{u}, \quad \text{(B5)}$$

with

$$F(u) = -2\pi\ln(|2q_0+u|)\frac{1+\frac{u}{q_0}}{u+2q_0}, \quad \text{(B6)}$$

$$G(u) = 2\pi\frac{1+\frac{u}{q_0}}{u+2q_0}. \quad \text{(B7)}$$

The functions $F(u)$ and $G(u)$ are analytic within the integration range and can be Taylor expanded. Restricting the expansion to first-order, one gets

$$\int_{-\Delta}^{\Delta} duF(0)\frac{1}{u} + G(0)\frac{\ln(|u|)}{u} + \int_{-\Delta}^{\Delta} duF'(0) + G(0)\ln(|u|). \quad \text{(B8)}$$

As $1/u$ and $\ln(|u|)/u$ are odd functions of u, the first two terms of Eq. (B8) are zero. The first contributing terms arise from $F'(0)$ and $G'(0)$,

$$F'(0)\int_{-\Delta}^{\Delta} du = 2F'(0)\Delta, \quad \text{(B9)}$$

$$G'(0)\int_{-\Delta}^{\Delta} du\ln(|u|) = 2G'(0)(\Delta\ln\Delta - \Delta), \quad \text{(B10)}$$

which show that the integral on the spherical shell behaves linearly with the width of the shell, as would any regular function do.

In the case of IR-inactive materials, the $1/q^2$ prefactors is not present. This makes the derivation easier since no angular dependence is present ($G(u) = 0$). The conclusion is nonetheless the same

$$F(u) = \frac{(1+\frac{u}{q_0})^2}{u+2q_0} = F(0) + F'(0)u + O(u^2), \quad \text{(B11)}$$

i.e., the first non-zero term in the integral of Eq. (B8) is linear in $2F'(0)\Delta$.

2. Integration of the $q = 0$ pole

For IR-inactive materials in the non-adiabatic approximation at a point different from the CBM or VBM, the function that should radially be integrated is

$$\Re\iiint_0^{q_c} dq^3\frac{1}{(q^2 - qq_0\cos\theta + \omega + i\delta)}. \quad \text{(B12)}$$

The last integral leads to

$$2\pi \int_0^{q_c} dq q^2 \int_0^{\pi} d\theta \frac{\sin\theta(q^2 - qq_0\cos\theta + \omega)}{((q^2 - qq_0\cos\theta + \omega)^2 + \delta^2)}, \tag{B13}$$

which gives the following radial integral:

$$2\pi \int_0^{q_c} dq \frac{q}{4q_0} \ln\left(\frac{(q^2 + 2qq_0 + \omega)^2 + \delta^2}{(q^2 - 2qq_0 + \omega)^2 + \delta^2}\right). \tag{B14}$$

When $\delta = 0$, this function behaves quadratically when q tends to 0 because the lowest order of the Taylor expansion of the logarithm is linear in q. Therefore, the integral on a sphere of radius Δ of this function is

$$\int_0^{\Delta} dq \frac{q}{4q_0} \ln\left(\frac{(q^2 + 2qq_0 + \omega)^2}{(q^2 - 2qq_0 + \omega)^2}\right) = C\Delta^3 + O(\Delta^4). \tag{B15}$$

However, for IR-active materials, the function to integrate is similar to a Lindhard function[97]

$$\frac{1}{4qq_0} \ln\left(\frac{(q^2 + 2qq_0 + \omega)^2 + \delta^2}{(q^2 - 2qq_0 + \omega)^2 + \delta^2}\right). \tag{B16}$$

This function actually tends to a finite value because of the linear behavior of the logarithm in q that cancels the denominator. Eq. (B16) for $\delta = 0$ gives

$$\int_0^{\Delta} \frac{1}{4qq_0} \ln\left(\frac{(q^2 + 2qq_0 + \omega)^2}{(q^2 - 2qq_0 + \omega)^2}\right) = A\Delta + O(\Delta^2). \tag{B17}$$

The same arguments also holds for the IR-active adiabatic case

$$\int_0^{\Delta} \frac{1}{2qq_0} \ln\left(\frac{2q_0 + q}{2q_0 - q}\right) = A\Delta + O(\Delta^3). \tag{B18}$$

3. Integration on a spherical shell around $q = 0$

In this section, we focus only on the δ-behavior of IR-active materials in the non-adiabatic framework, where Eq. (B16) has to be integrated.

The integrand has 3 poles: the first pole appears when $q = 0$ and the two second are the two real roots (if any) of $q^2 - 2qq_0 + \omega$, which we call q_1 and q_2 with $q_1 < q_2$.

Actually, when $q = 0$, the integrand does not diverge when $\delta \to 0$, as shown in Appendix B 2. We will therefore focus here on $q = q_2$ since the behavior with respect to δ at $q = q_1$ is similar.

The integration around q_2 is given by

$$2\pi \int_{q_2-\Delta}^{q_2+\Delta} dq \frac{1}{4qq_0} \ln\left(\frac{(q^2 + 2qq_0 + \omega)^2 + \delta^2}{(q^2 - 2qq_0 + \omega)^2 + \delta^2}\right). \tag{B19}$$

We introduce the change of variable $u = q - q_2$, and we consider $\delta \ll \Delta \ll q_2$,

$$2\pi \int_{-\Delta}^{\Delta} du \frac{1}{4q_2q_0} \ln\left(\frac{((q_1 + q_2)(2q_2))^2}{((q_2 - q_1)(u))^2 + \delta^2}\right). \tag{B20}$$

This integral can be expressed as

$$\frac{2\pi}{4q_2q_0}\left(2\Delta \ln\left(4(q_1 + q_2)q_2^2\right) - 2\Delta\ln(\delta^2) - \int_{-\Delta}^{\Delta} du \ln\left(\frac{u^2(q_2 - q_1)^2}{\delta^2} + 1\right)\right) \tag{B21}$$

and yields

$$\frac{2\pi}{4q_2q_0}\left(2\Delta \ln\left(4(q_1 + q_2)q_2^2\right) - 2\Delta\ln(\delta^2) - \frac{\delta}{q_2 - q_1}\frac{2\Delta(q_2 - q_1)}{\delta}\left(\ln\left(\frac{\Delta^2(q_2 - q_1)^2}{\delta^2} + 1\right) - 2\right) - \frac{\delta}{q_2 - q_1} 4\tan^{-1}\left(\frac{\Delta(q_2 - q_1)}{\delta}\right)\right). \tag{B22}$$

When Δ/δ is large, Eq. (B22) reduces to

$$\frac{2\pi}{4q_2q_0}\left(2\Delta \ln\left(4(q_1 + q_2)q_2^2\right) - 2\Delta\ln(\delta^2) - \frac{\delta}{q_2 - q_1} \times \frac{2\Delta(q_2 - q_1)}{\delta} 2\ln\left(\frac{\Delta(q_2 - q_1)}{\delta}\right) - \frac{\delta}{q_2 - q_1} 4\frac{\pi}{2}\right), \tag{B23}$$

which behaves as

$$C_1 - C_2\delta. \tag{B24}$$

The same procedure applies when $\omega = 0$. In this case, the poles are $q_1 = 0$ and $q_2 = 2q_0$. The ZPR convergence of a non-extremal eigenvalue of an IR-active material is thus linear with respect to δ in both the non-adiabatic and the adiabatic frameworks.

[1] P. Hohenberg and W. Kohn, Phys. Rev. **136**, B864 (1964).
[2] W. Kohn and L. J. Sham, Phys. Rev. **140**, A1133 (1965).
[3] R. D. Mattuck, *A Guide to Feynman Diagrams in the Many-Body Problem*, 2nd ed. (Dover Publications, 1976).
[4] G. D. Mahan, *Many-Particle Physics* (Springer, 2000).
[5] L. Hedin and S. Lundqvist, in *Solid State Physics*, edited by F. Seitz, D. Turnbull, and H. Ehrenreich (Academic Press, New York, 1969), Vol. 23, pp. 1–181.
[6] M. Shishkin, M. Marsman, and G. Kresse, Phys. Rev. Lett. **99**, 246403 (2007).
[7] M. Rohlfing and S. G. Louie, Phys. Rev. B **62**, 4927 (2000).
[8] F. Giustino, S. G. Louie, and M. L. Cohen, Phys. Rev. Lett. **105**, 265501 (2010).
[9] G. Antonius, S. Poncé, P. Boulanger, M. Côté, and X. Gonze, Phys. Rev. Lett. **112**, 215501 (2014).
[10] G. Onida, L. Reining, and A. Rubio, Rev. Mod. Phys. **74**, 601 (2002).
[11] S. Poncé, G. Antonius, Y. Gillet, P. Boulanger, J. Laflamme Janssen, A. Marini, M. Côté, and X. Gonze, Phys. Rev. B **90**, 214304 (2014).
[12] P. B. Allen and V. Heine, J. Phys. C: Solid State Phys. **9**, 2305 (1976).
[13] P. B. Allen and M. Cardona, Phys. Rev. B **23**, 1495 (1981).
[14] P. B. Allen and M. Cardona, Phys. Rev. B **27**, 4760 (1983).
[15] A. Marini, Phys. Rev. Lett. **101**, 106405 (2008).
[16] S. Poncé, G. Antonius, P. Boulanger, E. Cannuccia, A. Marini, M. Côté, and X. Gonze, Comput. Mater. Sci. **83**, 341 (2014).
[17] X. Gonze, P. Boulanger, and M. Côté, Ann. Phys. **523**, 168 (2011).
[18] E. Cannuccia and A. Marini, Phys. Rev. Lett. **107**, 255501 (2011).
[19] E. Cannuccia and A. Marini, Eur. Phys. J. B **85**, 1 (2012).
[20] A. Marini, S. Poncé, and X. Gonze, Phys. Rev. B **91**, 224310 (2015).
[21] B. Monserrat, N. D. Drummond, and R. J. Needs, Phys. Rev. B **87**, 144302 (2013).
[22] R. Ramírez, C. P. Herrero, E. R. Hernández, and M. Cardona, Phys. Rev. B **77**, 045210 (2008).
[23] M. Born and K. Huang, *Dynamical Theory of Crystal Lattices* (Oxford University Press, 1954).
[24] R. M. Sternheimer, Phys. Rev. **96**, 951 (1954).
[25] S. Zollner, M. Cardona, and S. Gopalan, Phys. Rev. B **45**, 3376 (1992).
[26] P. B. Allen, Phys. Rev. B **18**, 5217 (1978).
[27] G. Antonius, S. Poncé, E. Lantagne-Hurtubise, G. Auclair, X. Gonze, and M. Côté, "Dynamical and anharmonic effects on the electron-phonon coupling and the zero-point renormalization of the electronic structure," Phys. Rev. B (submitted); e-print arXiv:1505.07738 (2015).
[28] G. Grimvall, *The Electron-Phonon Interaction in Metals* (North-Holland Publishing Company, 1981).
[29] X. Gonze and C. Lee, Phys. Rev. B **55**, 10355 (1997).
[30] R. Zallen, R. M. Martin, and V. Natoli, Phys. Rev. B **49**, 7032 (1994).

[31]X. Gonze, Phys. Rev. B **55**, 10337 (1997).
[32]See supplementary material at http://dx.doi.org/10.1063/1.4927081 for the convergence studies.
[33]L. He, F. Liu, G. Hautier, M. J. T. Oliveira, M. A. L. Marques, F. D. Vila, J. J. Rehr, G.-M. Rignanese, and A. Zhou, Phys. Rev. B **89**, 064305 (2014).
[34]X. Gonze, B. Amadon, P.-M. Anglade, J.-M. Beuken, F. Bottin, P. Boulanger, F. Bruneval, D. Caliste, R. Caracas, M. Côté, T. Deutsch, L. Genovese, P. Ghosez, M. Giantomassi, S. Goedecker, D. Hamann, P. Hermet, F. Jollet, G. Jomard, S. Leroux, M. Mancini, S. Mazevet, M. Oliveira, G. Onida, Y. Pouillon, T. Rangel, G.-M. Rignanese, D. Sangalli, R. Shaltaf, M. Torrent, M. Verstraete, G. Zerah, and J. Zwanziger, Comput. Phys. Commun. **180**, 2582 (2009).
[35]S. Baroni, S. de Gironcoli, A. Dal Corso, and P. Giannozzi, Rev. Mod. Phys. **73**, 515 (2001).
[36]X. Gonze, G.-M. Rignanese, and R. Caracas, Z. Kristallogr. **220**, 458 (2005).
[37]G.-M. Rignanese, J.-P. Michenaud, and X. Gonze, Phys. Rev. B **53**, 4488 (1996).
[38]P. Boulanger, "Etudes *ab initio* des effets de la température sur le spectre optique des semi-conducteurs," Ph.D. thesis, Université Catholique de Louvain and Université de Montréal, 2010.
[39]A. Wright and J. Nelson, Phys. Rev. B **51**, 7866 (1995).
[40]A. Jain, S. P. Ong, G. Hautier, W. Chen, W. D. Richards, S. Dacek, S. Cholia, D. Gunter, D. Skinner, G. Ceder, and K. A. Persson, APL Mater. **1**, 011002 (2013).
[41]G. Yu, in *Properties of Advanced Semiconductor Materials: GaN, AlN, InN, BN, SiC, SiGe*, edited by M. E. Levinshtein, S. L. Rumyantsev, and M. S. Shur (John Wiley & Sons, 2001).
[42]I. Petrov, E. Mojab, R. C. Powell, J. E. Greene, L. Hultman, and J. Sundgren, Appl. Phys. Lett. **60**, 2491 (1992).
[43]H. Schulz and K. Thiemann, Solid State Commun. **23**, 815 (1977).
[44]W. R. L. Lambrecht and B. Segall, in *Properties of Group III Nitrides*, edited by J. H. Edgar (EMIS Datareviews Series, London, 1994).
[45]K. Kim, W. Lambrecht, and B. Segall, Phys. Rev. B **53**, 16310 (1996).
[46]C. Stampfl and C. Van de Walle, Phys. Rev. B **59**, 5521 (1999).
[47]G. Cappellini, G. Satta, M. Palummo, and G. Onida, Phys. Rev. B **64**, 035104 (2001).
[48]T. Sōma, A. Sawaoka, and S. Saito, Mater. Res. Bull. **9**, 755 (1974).
[49]J. Furthmüller, J. Hafner, and G. Kresse, Phys. Rev. B **50**, 15606 (1994).
[50]*Numerical Data and Functional Relationships in Science and Technology-Crystal and Solid State Physics, Vol. III of Landolt-Börnstein*, edited by O. Madelung (Springer, 1972).
[51]R. Wentzcovitch, K. Chang, and M. Cohen, Phys. Rev. B **34**, 1071 (1986).
[52]Y.-N. Xu and W. Ching, Phys. Rev. B **44**, 7787 (1991).
[53]X. Liu, L. Li, Q. Li, Y. Li, and F. Lu, Mater. Sci. Semicond. Process. **16**, 1369 (2013).
[54]G. Gildenblat and P. Schmidt, *Handbook Series on Semiconductor Parameters* (World Scientific, 1996), pp. 58–76.
[55]C. E. Patrick and F. Giustino, J. Phys.: Condens. Matter **26**, 365503 (2014).
[56]R. Wyckoff, in *Crystal Structures* (John Wiley & Sons, 1963), Vol. 1.
[57]M. Fuchs and M. Scheffler, Comput. Phys. Commun. **119**, 67 (1999).
[58]H. J. Monkhorst and J. D. Pack, Phys. Rev. B **13**, 5188 (1976).
[59]J. P. Perdew and A. Zunger, Phys. Rev. B **23**, 5048 (1981).
[60]M. Cardona and M. L. W. Thewalt, Rev. Mod. Phys. **77**, 1173 (2005).
[61]D. Vogel, P. Krüger, and J. Pollmann, Phys. Rev. B **55**, 12836 (1997).
[62]P. B. Perry and R. F. Rutz, Appl. Phys. Lett. **33**, 319 (1978).
[63]F. Litimein, B. Bouhafs, Z. Dridi, and P. Ruterana, New J. Phys. **4**, 64 (2002).
[64]N. E. Christensen and I. Gorczyca, Phys. Rev. B **50**, 4397 (1994).
[65]N. E. Christensen and I. Gorczyca, Phys. Rev. B **47**, 4307 (1993).
[66]A. Rubio, J. Corkill, M. Cohen, E. Shirley, and S. Louie, Phys. Rev. B **48**, 11810 (1993).
[67]C. Prasad and J. Dubey, Phys. Status Solidi B **125**, 629 (1984).
[68]N. L. Coleburn and J. W. Forbes, J. Chem. Phys. **48**, 555 (1968).
[69]R. Chrenko, Solid State Commun. **14**, 511 (1974).
[70]Y. Gillet, M. Giantomassi, and X. Gonze, Phys. Rev. B **88**, 094305 (2013).
[71]G. E. Jellison and F. A. Modine, Phys. Rev. B **27**, 7466 (1983).
[72]C. D. Clark, P. J. Dean, and P. V. Harris, Proc. R. Soc. A **277**, 312 (1964).
[73]S. Logothetidis, J. Petalas, H. M. Polatoglou, and D. Fuchs, Phys. Rev. B **46**, 4483 (1992).
[74]B. Monserrat, G. J. Conduit, and R. J. Needs, Phys. Rev. B **90**, 184302 (2014).
[75]Logothetidis *et al.* deduced the temperature dependence of the direct bandgap of diamond from first and second-derivative line-shape analysis, see Ref. 73 for more details.
[76]R. Pässler, Phys. Status Solidi B **216**, 975 (1999).
[77]J. P. Perdew and Y. Wang, Phys. Rev. B **45**, 13244 (1992).
[78]B. Monserrat and R. J. Needs, Phys. Rev. B **89**, 214304 (2014).
[79]W. Bludau, A. Onton, and W. Heinke, J. Appl. Phys. **45**, 1846 (1974).
[80]G. Macfarlane, T. McLean, J. Quarrington, and V. Roberts, Phys. Rev. **111**, 1245 (1958).
[81]P. Lautenschlager, P. B. Allen, and M. Cardona, Phys. Rev. B **33**, 5501 (1986).
[82]K. Karch and F. Bechstedt, Phys. Rev. B **56**, 7404 (1997).
[83]L. E. McNeil, M. Grimsditch, and R. H. French, J. Am. Ceram. Soc. **76**, 1132 (1993).
[84]O. Brafman, G. Lengyel, S. Mitra, P. Gielisse, J. Plendl, and L. Mansur, Solid State Commun. **6**, 523 (1968).
[85]P. Pavone, K. Karch, O. Schütt, D. Strauch, W. Windl, P. Giannozzi, and S. Baroni, Phys. Rev. B **48**, 3156 (1993).
[86]J. L. Warren, J. L. Yarnell, G. Dolling, and R. A. Cowley, Phys. Rev. **158**, 805 (1967).
[87]S. A. Solin and A. K. Ramdas, Phys. Rev. B **1**, 1687 (1970).
[88]G. Nilsson and G. Nelin, Phys. Rev. B **6**, 3777 (1972).
[89]P. Giannozzi, S. de Gironcoli, P. Pavone, and S. Baroni, Phys. Rev. B **43**, 7231 (1991).
[90]D. Brunner, H. Angerer, E. Bustarret, F. Freudenberg, R. Höpler, O. Dimitrov, R. Ambacher, and M. Stutzmann, J. Appl. Phys. **82**, 5090 (1997).
[91]Q. Guo and A. Yoshida, Jpn. J. Appl. Phys., Part 1 **33**, 2453 (1994).
[92]M. Cardona, Solid State Commun. **133**, 3 (2005).
[93]G. Nenciu, Rev. Mod. Phys. **63**, 91 (1991).
[94]R. W. Nunes and X. Gonze, Phys. Rev. B **63**, 155107 (2001).
[95]I. Souza, J. Íñiguez, and D. Vanderbilt, Phys. Rev. Lett. **89**, 117602 (2002).
[96]M. S. Hybertsen and S. G. Louie, Phys. Rev. B **35**, 5585 (1987).
[97]J. Lindhard, Mat.-Fys. Medd. K. Dan. Vidensk. Selsk. **28**, 1 (1954), available online at http://www.sdu.dk/media/bibpdf/Bind%2020-29%5CBind%5Cmfm-28-8.pdf.